Mineralium Deposita (2023) 58:1211–1235
https://doi.org/10.1007/s00126-023-01175-x

ARTICLE

Textural characterization of unidirectional solidification textures related to Cu–Au deposits and their implication for metallogenesis and exploration

Axel Müller[1,2] · **Doug Kirwin**[3] · **Reimar Seltmann**[2]

Received: 20 October 2022 / Accepted: 30 March 2023 / Published online: 20 April 2023
© The Author(s) 2023

Abstract

Ten rock samples with unidirectional solidification textures (USTs) from nine Asian and Australian porphyry and intrusion-related Au deposits and prospects were investigated in terms of mineralization sequences, textural and paragenetic relationships, melt and fluid inclusion inventory, cathodoluminescence, and trace elements of UST quartz. Despite general similar structural appearance of the investigated UST sequences, each UST locality has its own specific textural features. We provide a structural classification of observed USTs that distinguishes equigranular and heterogranular USTs, which are subdivided according to the UST layer structure into straight, wavy, or contorted/brain-like type. In addition, there is the group of disturbed USTs comprising incompletely developed UST layers, and ductile- or brittle-fragmented UST sequences. Ti-in-quartz-based calculations revealed crystallization temperatures of UST quartz between 590 and 770 °C. Primary silicate melt inclusions found in four samples indicate that quartz crystallized initially from a silicate melt. In five samples, fluid inclusion "boiling" assemblages were observed, documenting brine-vapor phase separation due to pressure drop. In one case, the "boiling" assemblage is in primary inclusions and in the other cases the assemblages have been trapped in pseudosecondary inclusions in a later stage. Primary brine inclusions without coeval vapor-rich inclusions were identified in one sample only. Our results permit UST formation in either an open-system setting where fluids exsolved from UST crystallization are periodically released by fracturing (pressure drops) after the formation of each individual UST layer, or closed-system setting where the exsolved fluids are trapped because of lack of fracturing as long the UST sequence forms. Here, the closed-system model is introduced for the first time to describe the formation of layered quartz UST sequences in porphyry systems where the open-system setting seems to be not applicable. Nonetheless, quartz UST sequences are very important exploration vectors for porphyry systems. Six out of the ten UST samples are high-grade with up to 12 g/t Au. However, in the investigated cases, the Au mineralization postdates UST formation. At Oyut Ulaan and Tampang, the UST quartz formation is co-genetic with major Cu–Fe sulfide mineralization, whereas in the other localities the UST formation predates the sulfide mineralization. In any case, UST layer sequences clearly functioned as an outer carapace and, thus, as a chemo-physical trap of passing mineralizing fluids entering the UST structure and may offer a vector to the main stockwork mineralization, which might occur 100 to 200 m above the UST zone.

Keywords Unidirectional solidification texture · Porphyry deposit · Quartz · Melt inclusion

Introduction

Unidirectional solidification textures (USTs) are recognized by exploration geologists in a variety of magmatic and transitional magmatic-hydrothermal ore deposits as pathfinders to economic mineralization (Shannon et al. 1982; Lowenstern and Sinclair 1996; Mustard 2001; Kirwin and Seltmann 2002; Kirwin 2005; Erdenebayar et al. 2014; Malekzadeh Shafaroudi et al. 2015; Seo et al. 2021; Bain et al. 2022). In a broader sense, USTs are

Editorial handling: K. Kelley

✉ Axel Müller
a.b.muller@nhm.uio.no

[1] Natural History Museum, University of Oslo, 0318 Oslo, Norway

[2] Natural History Museum, CERCAMS, Cromwell Road, London SW7 5BD, UK

[3] Consulting Geologist, Pathumtanee, Bangkok, Thailand

considered to be layers of hydrothermal or magmatic crystals with similar growth direction (unidirectional comb layers), perpendicular to lithological, geochemical, or mineralogical interfaces. As such, UST layers can be considered crystal growth fronts, which develop in veins and dykes or along contacts of sub-surface intrusions. In a strict sense, however, the term is applied here to banded, often pegmatitic, comb-like structures in the cupola of volatile-enriched granitic or porphyry stocks, with oriented quartz, feldspar, mica, amphibole, tourmaline, apatite, aegirine, or topaz crystals growing downward into the intrusion (Shannon et al. 1982; Kirkham and Sinclair 1988). These multiple comb layers, which are typically 1 mm to several centimeters or more in thickness, are cyclic and interlayered with magmatic aplitic to porphyritic facies (Fig. 1). The distinct and easily recognizable UST structure differentiates them from other features commonly observed in Au-bearing porphyry systems such as banded quartz veins. USTs sensu stricto have been increasingly recognized in different felsic intrusions throughout many orogenic belts around the world. They are associated with W and Mo, porphyry Cu and Au and intrusion-related Au, and REE mineralization.

Most authors agree that UST quartz layers in porphyries crystallized from an exsolved, magmatic fluid or melt that accumulated at the top of a shallow magma intrusion (Lowenstern and Sinclair 1996; Kirwin 2005; Seo et al. 2021). Such a liquid serves as a medium for rapid diffusion and transport of silica from the crystallizing magma to the growing quartz layers. The formation of multiple quartz UST layers may relate to variations in the P–T-X conditions of the fluids or melts from which they form. It is still debated if undercooling, depressurization, and/or boundary-layer processes at the crystallization front are the key driving forces of UST crystallization in these systems (e.g., Lowenstern and Sinclair 1996; Kirwin 2005; London 2009, 2014). USTs represent, however, only one type of crystallization texture associated with magmatic-hydrothermal mineralization in porphyry systems and should be seen in the genetic context. They occur together with aplitic, pegmatitic, miarolitic, and/or granophyric rock domains, massive quartz bodies (silica caps), breccia pipes, and mineralized stockworks (e.g., Fenn 1986; Kirkham and Sinclair 1988; London 1992; Candela and Blevin 1995; Candela 1997; Kirwin 2005; Carter and Williamson 2022) (Fig. 2). These features are, in general, indicative of melt immiscibility and related volatile exsolution and enrichment in the apical part of porphyry intrusions, which may lead to magmatic-hydrothermal mineralization (e.g., Candela 1997; Richards 2005; Seedorff et al. 2005; Sinclair 2007; Sillitoe 2010; Wilkinson 2013). Thus, the observation and understanding of such textures offer vectors for exploration geologists to locate and evaluate the ore-forming potential of porphyry systems. Some questions, however, remain regarding the genetic relationship of USTs and the porphyry mineralization.

In this study, ten UST samples from nine Asian and Australian porphyry and intrusion-related Au deposits and prospects were investigated in order to: (1) document and classify the diversity of USTs of Asian and Australian porphyry and intrusion-related Au deposits, (2) define their approximate formation conditions, (3) establish the crystallization sequence and genetic relationship between UST formation and main ore precipitation, (4) discuss the results in the light of existing models of closed- and open-system formations of quartz UST, and (5) assess their potential as textural pathfinders for economic mineralization. To achieve these goals, growth textures, melt and fluid inclusions, and trace elements of UST quartz were studied applying optical microscopy, scanning-electron microscopy (SEM), SEM cathodoluminescence (SEM-CL), microthermometry, energy-dispersive spectrometry(EDS), and electron probe micro-analyses (EPMA). The presented data are from an originally confidential report compiled for the mining company Ivanhoe Mines, Ltd., in 2004 and released for publication here to aid in an improved understanding of UST formation and to offer an exploration vector for porphyry-style mineralization.

Geological settings of sample material

Information about the geological setting of the sample locations, which are described in the following, is summarized in Table 1.

The Late Triassic (220–223 Ma; Ar–Ar mica; Lamb and Cox 1998) Cu–Mo–Au mineralized alteration zone of the Bayan Uul porphyry located in the Töv province in south Mongolia is exposed in an area of 3 by 5 km (Lamb and Cox 1998). A zone 300 by 900 m contains > 0.3 wt.% Cu and 0.005 wt.% Mo. The deposit consists of a quartz stockwork zone with pyrite, chalcopyrite, and molybdenite that occurs in or close to the porphyry intrusion. Quartz-tourmaline-chalcopyrite veins and quartz-tourmaline breccias are abundant (Lamb and Cox 1998). Advanced argillic and silica alteration at the surface suggests a relatively shallow porphyry system. The two investigated UST samples, a specimen with porphyry matrix (0.8 wt.% Cu, 12.2 g/t Au) and a tourmalinized sample, originate from the cupola of the porphyry intrusion 10 m from each other.

A well-preserved UST zone has been found near the contact of a quartz monzodiorite stock in drill hole OTD 183 at 289 m depth at the southwest Oyu Tolgoi Cu–Mo–Au deposit of the Oyu Tolgoi porphyry system (Perelló et al. 2001; Crane and Kavalieris 2012; Porter 2016). The upper part of the zone at the igneous contact features 2 m of a massive silica cap with an underlying 10 m interval of USTs

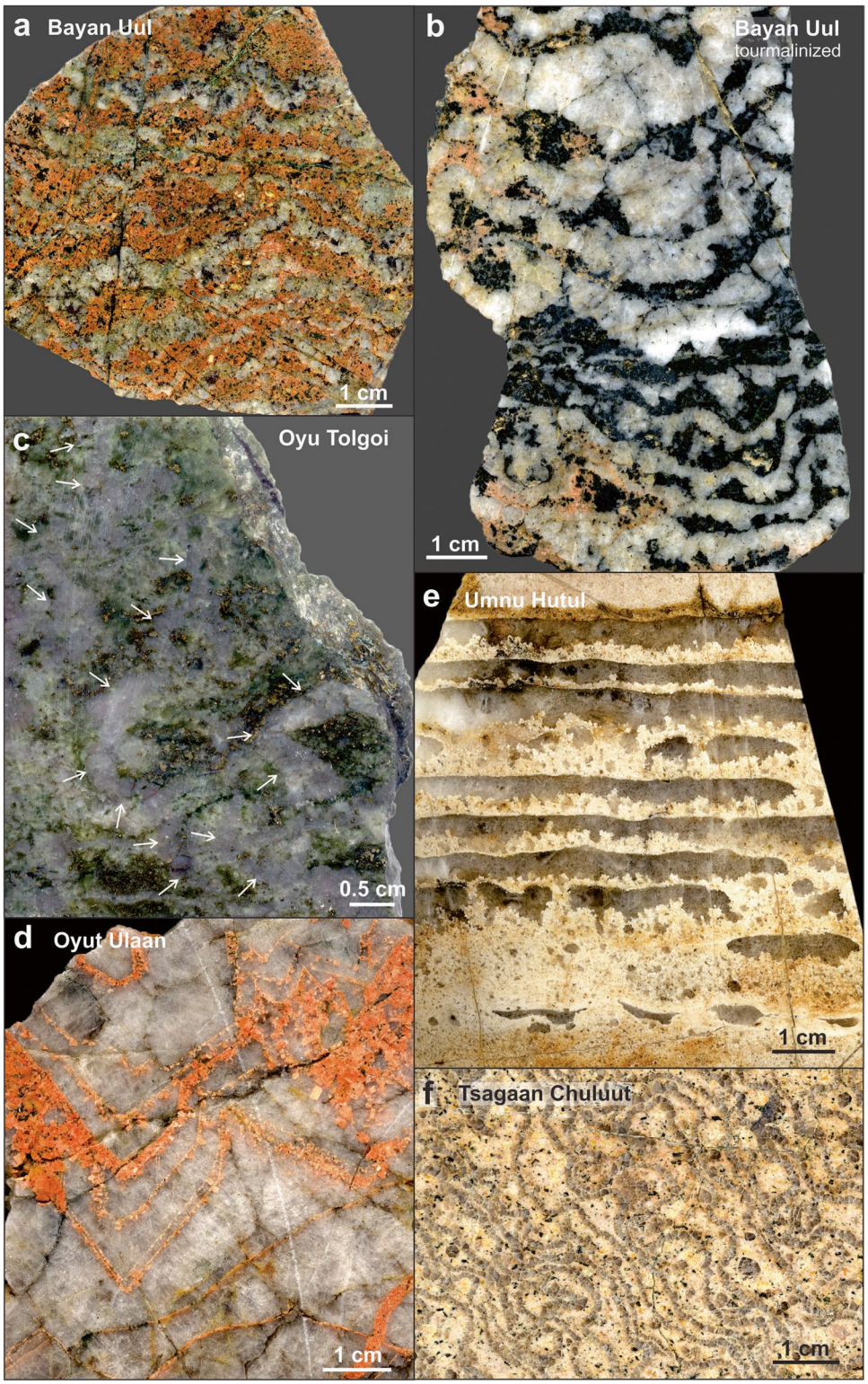

Fig. 1 Hand specimen photographs of UST. **a** Wavy, heterogranular UST quartz layers hosted by porphyritic rhyodacite from Bayan Uul. The black dots are pockets of microcrystalline tourmaline. **b** Wavy quartz USTs alternating with micro-crystalline tourmaline layers from Bayan Uul. In this specimen, the rhyodacite matrix is completely tourmalinized. **c** Contorted quartz USTs(arrows) in a monzonite host from Oyu Tolgoi Southwest. The monzonite matrix is intensely impregnated by magnetite, pyrite, and chalcopyrite. **d** Megacrystic quartz-K-feldspar UST from Oyut Ulaan. At growth zone boundaries, the crystals exhibit thin layers of tiny, pink K-feldspar crystals forming USTs within the UST quartz. **e** Straight quartz-aplite UST from Umnu Hutul. Some of the quartz UST lines are not completely developed. **f** Brain-textured, contorted quartz UST in dacite matrix from Tsagaan Chuluut. Quartz of the UST has consistent crystal size

(Kirwin et al. 2005). The UST layers are typically millimeters thick and highly contorted (brain texture). Eight meters of the UST zone in drill hole OTD183 assayed 0.25 g/t Au and 1.1 wt.% Cu (Table 1). Other USTs occur in the drill hole OTD514 in the Hugo Dummett zone where 2 m assayed 0.2 g/t Au and 3.3 wt.% Cu. Most of the sulfide mineralization crosscuts the UST quartz layers and the quartz veins. Sinuous quartz veins are commonly found throughout high-grade mineralization zones at Oyu Tolgoi; however, these are classified as "A veins" (Müller et al. 2010) according

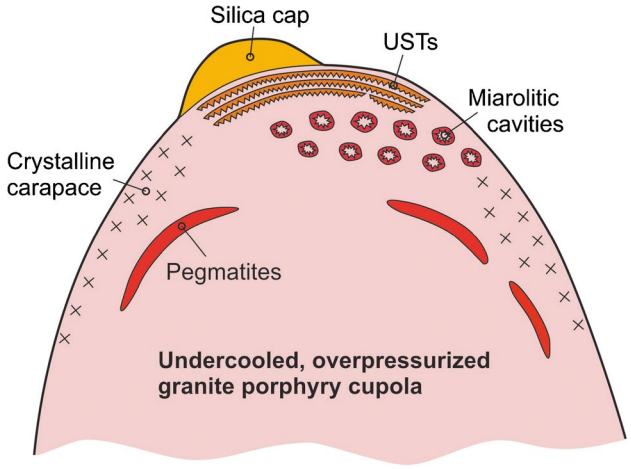

Fig. 2 Schematic diagram showing distribution of various early-stage magmatic textures in the apical zone of stock-like porphyry intrusions. Modified from Kirwin (2006)

to Gustafson and Hunt (1975). These are not considered to be USTs, although they may well have formed under high-pressure disequilibrium conditions.

The Oyut Ulaan Cu–Mo–Au porphyry prospect was explored by Ivanhoe Mines Ltd., in 2001–2002. In the course of geological mapping, USTs were identified at the "Aplite" locality (Kirwin 2005). The outcrop is relatively small with dimensions of 2 × 3 m. The USTs are multiphase rhythmic bands in which individual large quartz crystals also display internal quartz-feldspar growth zones. The USTs are hosted in an aplitic cupola. The area of mineralized wall rock (0.3–5.1 wt.% Cu and 0.0035–0.006 wt.% Mo) is about 250 × 700 m in size including skarns and a Cu-bearing tourmaline breccia-pipe complex.

Excellent examples of USTs were recognised in 2002 at the Umnu Hutul W–Mo deposit in far western Mongolia (Kirwin 2005). They occur as an annulus around an aplitic cupola, which is capped by a roof pendant of basic volcanic rocks. The UST zone has dimensions of 200 × 200 m and a thickness of up to 15 m. The textures vary considerably from distinctly parallel quartz bands to highly contorted layers, including atoll structures. In extreme cases, bands occur as clasts in an aplitic matrix. The thickness of individual quartz bands ranges from less than one mm to tens of cm. The ratio of quartz bands to intra-band aplite varies as well, with some examples being mostly quartz. Approximately 500 m SE of the UST occurrence, there is a quartz vein stockwork body approximately 150 m × 100 m, which has weak Mo and W mineralization.

The Tsagaan Chuluut district is located c. 200 km NNW of Choibolsan in the NE part of Mongolia. The district is a center of intense medium to large-scale alluvial Au mining activities. The regional geology is comprised of Jurassic granodiorite and quartz feldspar porphyry stocks and dioritic and gabbroic intrusions that are adjacent to graben bounding faults. Mesothermal Au- and Cu-bearing quartz veins are associated with one or more of the porphyry intrusions (Kirwin 2005). Cupolas of some of the quartz-feldspar porphyry stocks have been exposed, and well-preserved UST zones crop out as a cluster of small hills. The uppermost sections of the cupolas comprise massive silica bodies several cubic meters in size, which, in some cases, have UST features. Individual large zoned quartz crystals with c axis lengths exceeding 1 m have been observed. Other UST outcrops comprise more typical millimeter to centimeter thick contorted quartz layers within zones up to several metres thick and strike extents of tens to hundreds of meters. Atoll and cast textures are well developed where planar interfaces between UST layers have been exposed. The USTs at Tsagaan Chuluut appear unmineralized. However, they contain fine-grained hematite interpreted as pseudomorphs after magnetite.

The *Tampang* porphyry Cu–Au prospect (also known as the Bongkud) is located in northwestern Sabah, NE Borneo, approximately 65 km east of the state capital of Kota Kinabalu and 10 km east of the Mamut Cu–Au porphyry mine, which was active from 1975 to 1999. Exploration by Perilya Ltd. commenced in 1996 and led to the discovery of the Tampang porphyry Cu–Au system through the observation of an outcropping quartz stockwork veining (Kirwin 2001). The monzonitic porphyry system is part of the Kinabalu Magmatic Zone emplaced in the Sabah Orogenic Belt during the late Miocene in a late-orogenic, extensional setting. The plutons comprising the Kinabalu Magmatic Zone at the Mamut mine are I-type intrusions and are coarsely plagioclase phenocrystic monzonites and diorites. Micromonzonites are associated with the mineralization at Tampang. USTs are commonly observed in the Tampang micromonzonite in weathered outcrops and drill cores (Kirwin 2001). They occur as millimeter to tens of centimeter thick bands over repeated intervals up to 3 to 5 m. They are commonly well-mineralized with 1 to 2 wt.% Cu and up to 3 g/t Au (Table 1) (Kirwin 2001).

The Hada Sumu UST sample originates from a Cu–Au prospect in the Saihan Ta La region of Inner Mongolia. The outcropping USTs have high Au grades containing up to 12 g/t Au (Forbes et al. 2003), and the UST zone was mined for Au (Kirwin 2005). The prospect occurs close to the Bilihe Au mine where USTs are also present (Huang et al. 2020), both localities are part of the Saihan Ta La Au district. Aplites with USTs consisting only of magnetite crystal layers have also been found at Hada Sumu (Kirwin 2005).

The Kidston Au deposit (140 t Au) is hosted within a trapezoid-shaped breccia pipe with surface dimensions of 1100 × 900 m, extending to a depth of 1400 m (Baker and Andrew 1991). Brecciation and Au mineralization are spatially and temporally related to a swarm of Permo-Carboniferous

Table 1 Characterization of the sampled porphyry and IRGD deposits

Location Coordinates	Province/country	Type/subtype (according to Sinclair 2007)	Host orogen	Formation age	Formation depth/ pressure	Total ore tonnage [Mt]	Grade of the deposit	Grade of the UST sample	References
BayanUul 46° 37′ 20″ N 104° 54′ 03″E	Töv/Mongolia	Porphyry/Cu–Mo–Au	Central Asian Orogenic Belt	220–223 Ma (Ar–Ar biotite)	n.d	Prospect	> 0.3 wt.% Cu 0.005 wt.% Mo	12.2 g/t Au, 0.8 wt.% Cu	Koval et al. (1988), Lamb and Cox (1998)
Oyu Tolgoi 43° 01′ 30″N 106° 52′ 31″E	Ömnögovi/Mongolia	Porphyry/Cu–Mo–Au	Kazakh-Mongol magmatic arc of the central Asian Orogenic Belt	372 ± 1.2 Ma (Re-osmolybdenite), 372 ± 3 Ma (method not provided)	~ 3.5 km/ ~ 1 kbar	3,755	Cu 0.98% Mo 0.01% Au 0.38 g/t	0.25 g/t Au, 1.1 wt.% Cu	Perelló et al. (2001), Kirwin et al. (2005), Zhang et al. (2006), Khashgerel et al. (2009), Müller et al. (2010), Crane and Kavalieris (2012), Porter (2016)
Oyut Ulaan 44° 34′ 50″N 109° 25′ 5″E	Dornogovi/Mongolia	Porphyry/Cu–Mo–Au	Central Asian Orogenic Belt	330 ± 0.5 Ma (U–Pb zircon)	n.d	Prospect	0.3–5.1 wt.% Cu, 0.0035–0.006 wt.% Mo	Traces of Cu	Kirwin (2005), Blight et al. (2010)
Umnu Hutul 48° 28′ 14″N 89° 49′ 04″E	West Mongolia/ Mongolia	Porphyry/W–Mo	Central Asian Orogenic Belt	n.d	n.d	Prospect	n.d	Traces of W, Bi, Nb, Ta, and Sn	Kirwin (2005)
Tsagaan Chuluut 49° 29′ 03″N 113° 26′ 34″E	Erdenet/Mongolia	Porphyry/Cu–Au	Central Asian Orogenic Belt	~ 290 Ma	n.d	Prospect	n.d	Not mineralized	Kirwin (2005)
Tampang 6° 03′ 04″S 116° 43′ 42″E	Sabah/Borneo	Porphyry/Cu–Au	Miocene Sabah Orogenic Belt	6.7 to 8.3 Ma (K–Ar biotite)	n.d	Prospect	n.d	1 to 2 wt.% Cu, up to 3 g/t Au	Kirwin (2001)
Hada Sumu 42° 25′ 05″N 113° 34′ 35″E	Inner Mongolia/ China	Porphyry/Cu–Au	Central Asian Orogenic Belt	n.d	n.d	Prospect	n.d	12 g/t Au	Forbes et al. (2003)
Kidston 18° 52′ 39″S 144° 09′10″E	Queensland/Australia	Intrusion-related Au deposit	Carboniferous back-arc magmatism at the eastern edge of the Australian Craton (Georgetown Inlier)	335.7 ± 4.2 Ma (U–Pb zircon)	~ 3.5 km/ ~ 1 kbar	42.6	Au 1.43 g/t Ag 1.85 g/t	Native Au and traces of Cu	Baker and Andrew (1991), Murgulov et al. (2009)
Ridgeway 33° 27′ 52″S 149° 00′ 10″E	New South Wales/Australia	Porphyry/Cu–Au	Lachlan Orogenic Belt	456.9 ± 7.2 Ma (U–Pb titanite), 455.8 ± 4.4 Ma (U–Pb zircon)	< 3 km/ < 0.9 kbar	154	Cu 0.385% Au 0.73 g/t Ag 0.81 g/t	Cu-rich	Holliday et al. (2002), Wilson et al. (2003, 2007)

n.d., not determined

rhyolite dikes, which intruded Mesoproterozoic metamorphic and Siluro-Devonian granitoid host rocks at 335.7 ± 4.2 Ma (Murgulov et al. 2009). The rhyolite dikes are interpreted as being underlain by a Permo-Carboniferous batholith. Three main mineralization stages have been distinguished within the Kidston breccia pipe (Baker and Andrew 1991). Stage 1 comprises pre-breccia USTs and uneconomic Cu-Mo stockwork veins, partially tourmalinized in the carapaces of small rhyolite stocks. Stage 2 comprises the main brecciation resulting in the fragmentation porphyry and the associated USTs and stockwork. The UST specimen described in this study is a tabular breccia fragment of stage 1. Stage 3 postdates the breccia formation and resulted in economic-grade Au mineralization. The mineralization is in replacement cavities in the breccia matrix and sheet veins that cut the breccia. The structural control on the distribution of post-breccia mineralization was an inverted funnel-shaped zone of enhanced permeability produced by the forceful emplacement of a post-breccia rhyolite into the lower portion of the breccia pipe. The investigated UST breccia clast originates from the high-grade Au-mineralized zone.

Ridgeway Cu–Au porphyry deposit (54 Mt at 2.5 g/t Au and 0.77% Cu) occurs within the Cadia district of New South Wales, Australia, which consists of a cluster of four Late Ordovician Au–Cu porphyries and two Fe–Cu–Au skarn deposits (Holliday et al. 2002; Wilson et al. 2003). The deposits are aligned along a 7-km-long, northwest-oriented corridor of alteration and mineralization related to an Ordovician alkalic intrusive complex of monzonitic composition associated with the Macquarie arc of the Lachlan Orogenic Fold Belt (Wilson et al. 2007). Multiple events of quartz-sulfide veining and related calc-potassic (actinolite-magnetite-biotite) to potassic (biotite-orthoclase) alteration are associated with at least three stages of intrusion. Alteration and mineralization are concentrically zoned around this intrusive complex. A core of calc-potassic to potassic alteration passes upward and outward to propylitic and local sodic alteration. Sulfide assemblages change from a bornite-rich core, through a chalcopyrite-rich zone, to a pyrite-bearing periphery (Wilson et al. 2003). A sequence of USTs was exposed in the Cadia-Ridgeway underground mine about 450 m below surface. The UST sequence comprises at least twelve 0.3- to 30-cm-thick layers of comb quartz + magnetite ± chalcopyrite ± pyrite alternating with monzonite layers with a total thickness of 1.4 m and a strike extent of at least 30 m at the cupola of an intermineral-stage monzonite intrusion (Wilson et al. 2003).

Methods

Scanning electron microscopy and scanning electron microscope cathodoluminescence

Back-scattered electron imaging (BSE) and phase identification were carried out on a JEOL 5900 LV scanning electron microscope (SEM) equipped with an Oxford Instruments INCA energy-dispersive spectrometer (EDS) system operated at 20 kV. The instrument is based at the Natural History Museum London. SEM-CL analyses were obtained from the same device using a GATAN MiniCL detector. The applied acceleration voltage and current was 20 kV and ~ 1 nA, respectively. The CL images were collected from 4 scans of 20-s photo speed each and a processing resolution of 1280 by 960 pixels and 256 grey levels. Qualitative spectra of minerals were obtained by the OXFORD INCA EDX detector attached to the analytical SEM. The acquisition time of energy-dispersive spectra was 30 s.

Electron probe microanalyses

Trace element contents of Al and Ti in quartz were analyzed with a Cameca SX50 electron microprobe at the Natural History Museum (NHM) London. For high precision and sensitivity, a beam current of 200 nA, a beam diameter of 5 µm, and counting times of 15 s for Si and of 300 s for Al and Ti were chosen. Limits of detection (LOD) were (3 σ of single point background) 16 ppm for Al and 29 ppm for Ti.

Fluid inclusion microthermometry

The samples prepared as doubly polished "thick" (~ 200 µm) thin sections for CL were demountable and usable as fluid inclusion "wafers." Sections were scanned for suitability for fluid inclusion microthermometry, and sections were chosen for study based on the petrographic work. Microthermometry was carried out using the joint Imperial College London/NHM facility comprising a Linkam THC600 heating/freezing stage attached to an Olympus Optiphot microscope with a Nikon × 50 long working distance lens. Calibration on the instrument was regularly monitored using standard artificial inclusion wafers. The provided homogenization temperatures are uncorrected for pressure and thus represent minimum temperatures for formation. However, in the case of inclusions where boiling is suspected during trapping, homogenization temperatures are, by definition, the trapping temperature.

Heating experiments on melt inclusions

The heating experiments of crystallized melt inclusions were run in an electric muffle furnace (Lenton Thermal Designs) at 1 atm at 50 °C steps between 500 and 1100 °C. Each experiment was run for 6 h. After each heating step, the melt inclusions in the quartz wafers were checked if melting or homogenization or other modifications had occurred, in this way the temperature of starting melting T_m and the temperature of partial homogenization T_h (silicate glass + vapor phase). We interpret that the determined homogenization temperatures T_h reflect approximately the

formation temperature of the quartz hosting the melt and fluid inclusions.

Results

UST description and mineralogy

This section describes the hand-specimen- and microscope-scale UST quartz textures and associated mineralogy, which are summarized in Table 2. The UST from Bayan Uul forms wavy, heterogranular, and semi-parallel quartz layers (Fig. 1a and b). The thickness of the quartz layers varies from 0.1 to 2 cm. The layers alternate with a fine-grained, weakly porphyritic rhyodacite. The potassic altered host rock consists of K-feldspar, albite, muscovite, chlorite, and quartz (Table 2). Pseudomorphs of secondary Fe and Fe–Cu oxides after sulfides are locally enriched at the contact between UST quartz and host rock in UST growth direction (Fig. 3a). In the tourmalinized UST sample (Fig. 1b), the groundmass consists mainly of fine-grained tourmaline needles replacing the minerals of the rhyodacite. Textural relationships indicate that the tourmalinization postdates the UST formation (Table 2) but predates the sulfide mineralization. Figure 3b illustrates that sulfide overgrew the tourmaline needles. In SEM-CL, the UST quartz shows weakly contrasted, oscillatory growth zoning overprinted by a dense network of dull-luminescent, healed quartz veins of different generations (Fig. 3c). An older micro-vein generation contains tourmaline representing the tourmalinization stage, and a younger vein generation with chlorite and sulfides representing the mineralization stage. Native Au could not be identified in the two Bayan Uul UST samples despite a gold content of 12 g/t.

The UST from the Oyu Tolgoi Southwest porphyry deposit comprises strongly contorted and boudinaged (ductile fragmented) quartz bands with a variable thickness of 0.5 to 10 mm (Figs. 1c and 3d). In SEM-CL, the UST quartz shows weakly contrasted growth zoning and a dense network of healed, dull luminescent fractures (Fig. 3e). The quartz bands are embedded in a fine-grained, multiple altered porphyry matrix of K-feldspar, sericite, pyrophyllite, quartz, and biotite (Table 2). The sample is intensely mineralized with magnetite, pyrite, and chalcopyrite (Figs. 1c and 3d). Magnetite crystallization is co-genetic with the UST formation but predates the formation of pyrite and chalcopyrite (Table 2). Brecciated pyrite is healed by chalcopyrite. The sulfide crystallization stage, overprinting the UST, is associated with the dissolution of UST quartz and precipitation of a new, dull luminescent quartz generation (qtz2 in Fig. 3g).

The sample from the Oyut Ulaan prospect (Fig. 1d) comprises two comb quartz crystals about 10 cm in length originating from heterogranular multi-layer UST sequence with crystals sizes of about 1 to 25 cm. At growth zone boundaries, the crystals exhibit thin layers of tiny, pink K-feldspar crystals forming USTs within the UST quartz. The K-feldspar layers are, however, not exclusively made of euhedral K-feldspar crystals. In some places, the K-feldspar is embedded in aplite with accessory biotite (altered to chlorite), zircon, and rutile. The K-feldspar layers also pseudomorphs of secondary FeO and Fe–CuO minerals after Fe–Cu sulfides. Growth zoning within the UST quartz could not be revealed by SEM-CL. The quartz exhibits a dense and multi-stage network and pattern of healed and recrystallized quartz with different CL intensities interpreted as fluid pathways and recrystallization textures.

The quartz UST of Umnu Hutul W–Mo porphyry prospect comprises straight, rhythmic equigranular quartz layers alternating with a granitic aplite (Fig. 1e). Some of the quartz layers appear incomplete probably due to the local lack of SiO_2 in some growth stages (see lower part of Fig. 1e). The UST quartz of Umnu Hutul is the only studied sample that had very low CL intensity without any CL contrasts or structures. The partially sericitized aplite consists mainly of K-feldspar, albite, and muscovite. Beside accessory topaz and xenotime, the aplitic host contains tiny (< 50 µm) W, Bi, Nb, Ta, and Sn oxide minerals. The structural features indicate that the UST layers crystallized co-genetic with the aplite layers.

The strongly contorted, worm-like, equigranular UST layers from the Tsagaan Chuluut prospect constitute a brain-like texture embedded in a fine-grained, porphyritic rhyolitic-quartzdacitic matrix (Fig. 1f, Table 2). The UST layers consist of more or less isometric quartz crystals with consistent crystal size of about 2 mm forming UST bands of consistent thickness (Fig. 5a). Chlorite pseudomorphs after amphibole and biotite are occasionally aligned parallel to the UST layers (Fig. 5a), indicating that the porphyry melt was still viscous when the UST formed. Primary growth zoning could not be detected clearly with SEM-CL within the overall bright luminescent UST quartz. Along some quartz grain boundaries, however, irregular, slightly duller luminescent grain margins were observed (Fig. 5b).

UST quartz from Tampang forms small contorted and boudinaged (ductile fragmented) bands with a thickness of 2 to 5 mm in a Cu–Au mineralized porphyry matrix (Fig. 4a). The porphyry matrix, consisting of K-feldspar, quartz, and chlorite, underwent phyllic quartz-sericite-ankerite alteration and hosts abundant chalcopyrite. Large (up to 500 µm), euhedral to subhedral chalcopyrite may be co-genetic with the UST quartz because it occurs commonly as inclusions in quartz (Fig. 5c and d). Native Au (10 µm) was identified in a sericite micro-pocket in K-feldspar. In SEM-CL, the UST quartz exhibits fine, oscillatory growth zoning (Fig. 5c). The primary growth pattern is almost free of secondary structures typically observed in the other investigated UST quartz samples. A few K-feldspar veins were associated with

Table 2 Textures of UST samples

Locality	UST characteristics	CL properties of UST quartz	Pre-UST paragenesis of the porphyry matrix	UST paragenesis/mineralization	Post-UST paragenesis/mineralization
Bayan Uul	Multiple, wavy, heterogranularqtz layers 0.1 to 2 cm thick in porphyry matrix	Primary oscillatory growth zoning with bright CL, dense network of microcracks healed with qtz with dull CL associated with tourmalinization and sulfide mineralization	Kfs, ab, qtz, ms	Qtz	1) Tur, rt, ap, qtz with dull CL 2) Py and ccp (subsequently altered to FeO and FeCuO oxides), chl, qtz with dull CL
Oyu Tolgoi	Multiple, strongly contorted, heterogranular and ductile fragmented qtz layers 0.5 to 10 mm thick in porphyry matrix	Relict primary oscillatory growth zoning, dissolution/precipitation of qtz with low CL associated with sulfide mineralization overprinting UST qtz	Kfs, qtz, bt	Qtz, mt	Py, ccp, ser, prl, brt, qtz with dull CL
Oyut Ulaan	Multiple, straight, heterogranular quartz layers 1 to 25 cm thick with intra-crystal kfs micro-UST along individual qtz growth zones in co-genetic aplite matrix	Bright CL without primary zoning, multistage microcracks healed with dull CL and hosting large fluid inclusions	-	UST: Qtz Co-genetic micro-UST: Kfs and co-genetic aplite: ab, zrn, rt, altered bt, py, and ccp	-
Umnu Hutul	Multiple, straight, equigranularqtz layers up 0.5 to 1 cm thick alternating with co-genetic aplite layers	No CL	-	UST: Qtz Co-genetic aplite: kfs, qtz, ab, mus, toz, xtm, W-, Bi, Nb-, Ta-, and Sn oxides	-
Tsagaan Chuluut	Multiple, strongly contorted, brain-like qtz bands about 2 mm thick in porphyry matrix	Bright CL but no primary growth zoning, diffusion rims at grain margins with dull CL	Kfs, ab, qtz, bt, chl, zrn, rt, ap, mt	Qtz	-
Tampang	Multiple, strongly contorted, equigranular and ductile fragmented qtz layers 2 to 5 mm thick in porphyry matrix	Primary oscillatory growth zoning, very few secondary structures	Kfs, qtz, chl	Qtz, ccp, ga, teh, bis, Ag-Pb tellurides and selenides	Second generation of ccp, qtz, ser, ank, native Au
Hada Sumu	Multiple, wavy, heterogranularqtz layers 0.1 to 1 cm thick alternating with granophyric kfs-qtz layers	Bright CL with some primary growth zones, granophyric qtz overgrowth with very bright CL	Kfs, ab, qtz, chl	UST: Qtz,mt Co-genetic granophyric qtz-kfs intergrowth,	-
Kidston	Multiple, wavy, equigranular and brittle fragmented qtz layers 0.2 to 2 cm thick in porphyry matrix	Bright CL without primary zoning, dendritic qtz overgrowth with dull CL	Kfs, qtz, ms, zrn, rt, xtm, mnz	Qtz	Dendritic qtz overgrowths with dull CL, py, ccp, ser, native Au, supergene overprint resulting in cv formation

Table 2 (continued)

Locality	UST characteristics	CL properties of UST quartz	Pre-UST paragenesis of the porphyry matrix	UST paragenesis/mineralization	Post-UST paragenesis/mineralization
Ridgeway	Multiple, contorted, incomplete developed, heterogranular and ductile fragmented qtz layers 0.3 to 5 cm thick in porphyry matrix	Bright Cl with fine oscillatory growth zoning, dense network of microcracks healed with qtz with dull CL associated with tourmalinization and sulfide mineralization	Kfs, ab, qtz, chl	Qtz, mt	Py, ccp, qtz, chl

Abbreviations: *ab*, albite; *ank*, ankerite; *ap*, apatite; *brt*, barite; *bis*, bismuthinite; *bt*, biotite; *chl*, chlorite; *cv*, covellite; *ccp*, chalcopyrite; *fl*, fluorite; *ga*, galena; *hm*, hematite; *kfs*, potassium feldspar; *mt*, magnetite; *mnz*, monazite; *ms*, muscovite; *prl*, pyrophyllite; *py*, pyrite; *qtz*, quartz; *rt*, rutile; *ser*, sericite; *sph*, sphalerite; *teh*, tetrahedrite; *toz*, topaz; *tur*, tourmaline; *xtm*, xenotime; *zrn*, zircon

a second anhedral and smaller generation of chalcopyrite cut the UST quartz (Fig. 5c).

The UST quartz from Hada Sumu forms wavy layers together with paragenetic magnetite crystals alternating with micro-granophyric K-feldspar-quartz layers in a quartz porphyry matrix (Fig. 4b, Table 2). Magnetite up to 5 mm in size is common and co-genetic with the UST quartz forming combined quartz-magnetite UST or magnetite only UST (Fig. 4b and c). Granophyric K-feldspar-quartz textures occur preferentially in wavy layers parallel to the quartz UST layers, enhancing the layered structure of the rock. The K-feldspar-rich bands occasionally contain incomplete developed comb quartz layers. In SEM-CL, the dull luminescent comb quartz shows some growth zoning and overgrowths of fine-grained granophyric quartz with high CL intensity (Fig. 6a and b).

The sample from Kidston represents a UST clast found within the Kidston breccia pipe. The length of the comb quartz crystals in the wavy UST of this sample ranges between 0.2 and 2 cm (Fig. 4d, Table 2). Baker and Andrew (1991) reported UST quartz crystal sizes of up to 1 m. The USTs are hosted by strongly phyllic altered, fine-grained quartz-feldspar porphyry. Major minerals are K-feldspar, quartz, and muscovite with accessory zircon, rutile, xenotime, and monazite (Table 2). Ore minerals include chalcopyrite, covellite, and native Au. Chalcopyrite occurs dispersed in the porphyry matrix or along thin, healed veins crosscutting the UST (Fig. 6c) and thus superimposes the UST. Covellite partially replaces chalcopyrite along grain boundaries, implying supergene Cu enrichment. Native Au up to 10 µm in size occurs in micro-cavities in the porphyritic matrix only (Fig. 6d) post-dating the UST as well as the Cu–Mo mineralization stages. The CL intensity of the UST quartz is relatively low, and no primary growth zoning was detected (Fig. 6e). The UST crystal shown in Fig. 6e has a dendritic overgrowth with very low CL intensity. Two populations of quartz-healed microcracks crosscut the UST quartz: an older non-luminescent microvein population with chalcopyrite inclusions (see also Fig. 6c) and a younger dull-luminescent population.

The contorted heterogranular quartz USTs from Ridgeway are hosted by chloritized porphyry matrix of monzonitic composition (Fig. 4e). In some parts, the quartz UST layers seem to be fragmented during or shortly after their formation in a still viscous reacting magmatic matrix. UST quartz contains euhedral inclusions of magnetite. In some cases, magnetite is intergrown with UST quartz, implying that UST quartz and magnetite are co-genetic. In other cases, magnetite is the only UST-forming mineral. In SEM-CL, UST quartz shows fine-scale, growth zoning

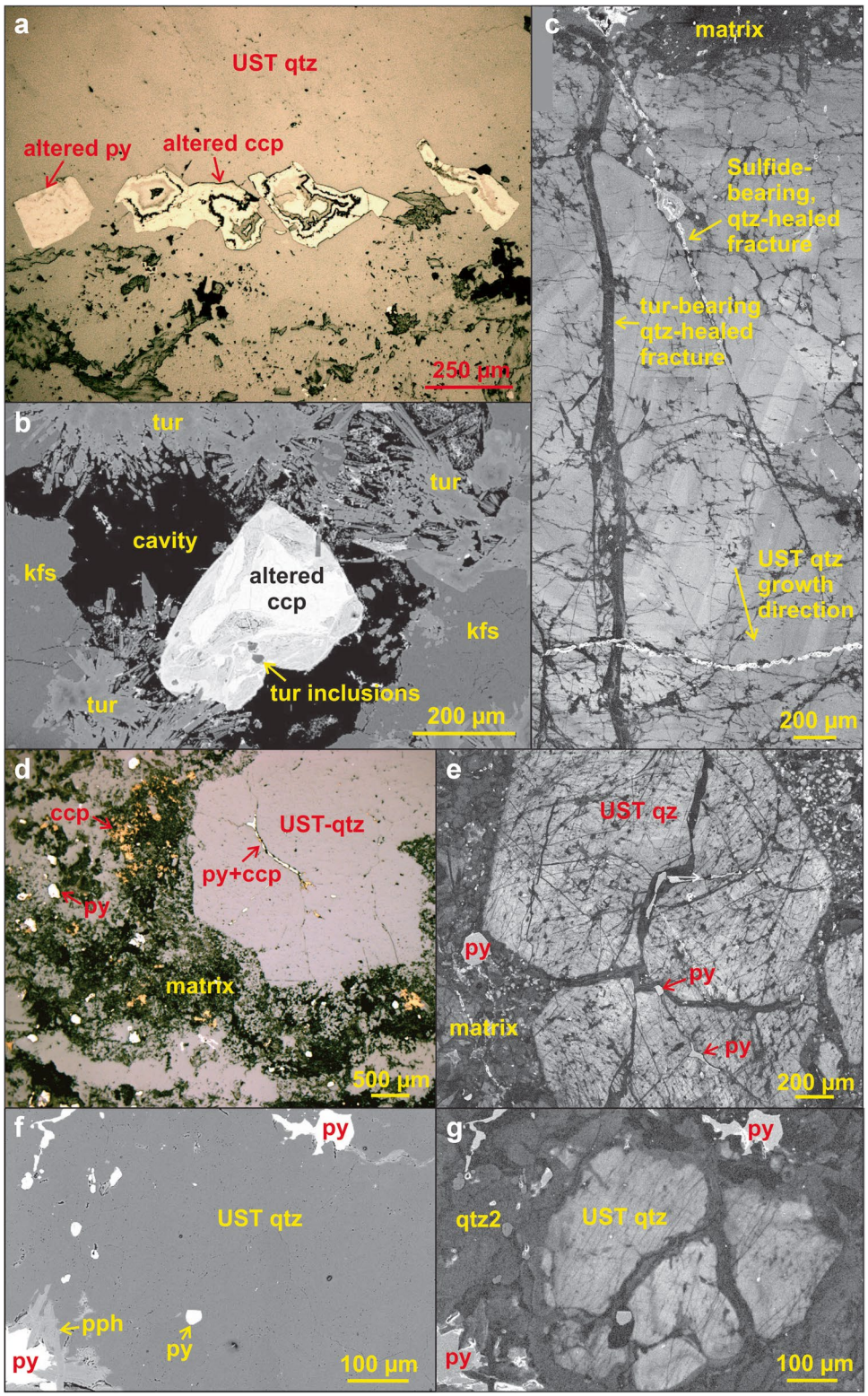

Fig. 3 Photomicrographs of textures observed in the Bayan Uul and Oyu Tolgoi UST samples. **a** Reflected light image showing altered pyrite (py) and chalcopyrite (ccp) aligned at the growth front of a Bayan Uul UST layer. **b** Altered chalcopyrite (ccp) crystal in a tourmaline-framed (tur) cavity and with tourmaline inclusions. The textures are indicative that the chalcopyrite crystallized after tourmaline formation. Bayan Uul. **c** SEM-CL image of Bayan Uul UST quartz with bright CL and weakly contrasted growth zoning. An older generation of dull-luminescent, tourmaline-bearing quartz microveins and a younger generation of sulfide-bearing microveins transect the UST quartz. **d** Combined reflected light/plane light optical microscope image showing a folded, wormy Oyu Tolgoi UST quartz band. Pyrite (py) and chalcopyrite (ccp) are abundant in the porphyry matrix and along micro-cracks transecting USTs and, thus, postdating the UST quartz formation. **e** SEM-CL image of Oyu Tolgoi UST quartz with bright CL. The quartz shows a dense network of microfractures healed with dull luminescent quartz. The larger fractures contain pyrite (py). **f** BSE image of a Oyu Tolgoi UST quartz layer, which appears homogenous applying this imaging method, with pyrite(py) and pyrophyllite (pph). **g** SEM-CL image of the area shown in (**f**). The bright luminescent UST quartz shows strong replacement by younger, dull luminescent quartz (qtz2), which cannot be distinguished applying BSE (**f**). The dull luminescent quartz is cogenetic with the pyrite precipitation post-dating the UST formation

of low CL contrast (Fig. 7a). Micro-veins of the quartz-chlorite-pyrite-chalcopyrite assemblage crosscut the UST and porphyry matrix postdating the UST quartz-magnetite stage (Fig. 7c and d).

Micro-inclusions in UST quartz

The micro-inclusion inventory of UST quartz focuses on primary and pseudosecondary inclusions (Table 3). Criteria

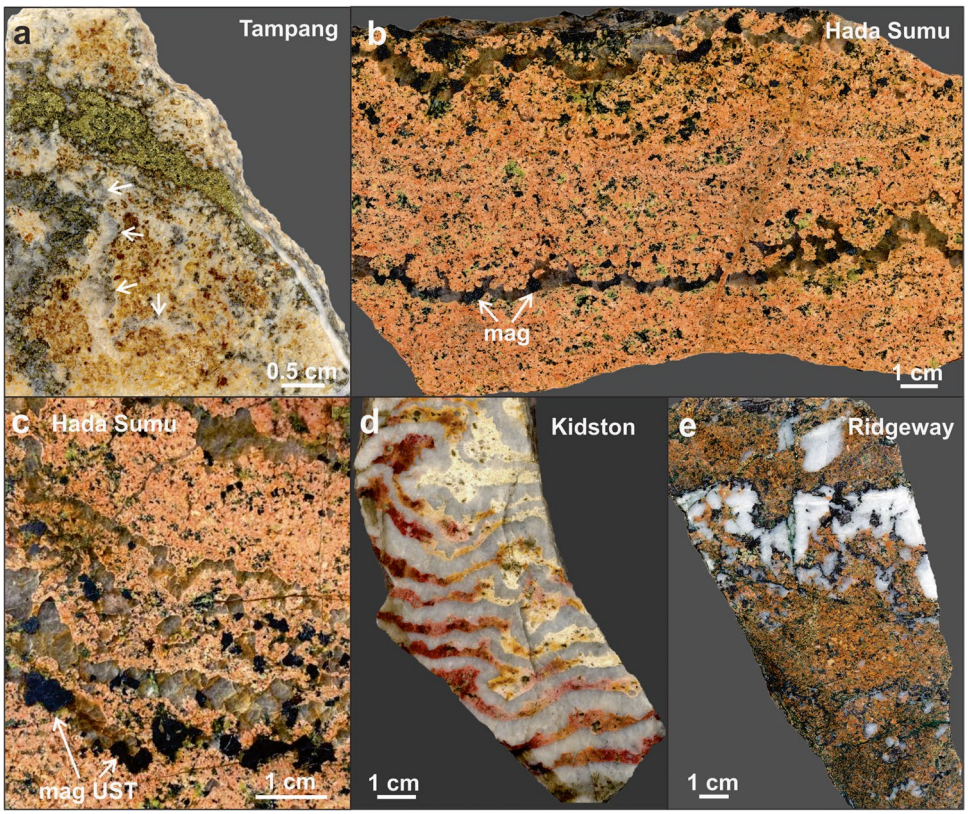

Fig. 4 Hand specimen photographs of USTs. **A** Contorted, fragmented quartz UST layer from Tampang in a Cu–Au mineralized, phyllic-altered porphyry matrix. The arrows are pointing to the UST layer. In the upper part of the specimen is a layer of massive chalcopyrite, which is co-genetic with the UST quartz (see also Figs. 5c and d).**b** Wavy quartz and quartz-magnetite UST alternating with granophyric K-feldspar UST from Hada Sumu in a quartz porphyry matrix. Magnetite up to 5 mm in size is common and co-genetic with the UST quartz. **c** Detail of another Hada Sumu sample with magnetite (mag) UST layer at the bottom of the image. **d** Rhythmic, wavy quartz UST in strongly phyllic altered, fine-grained quartz-feldspar porphyry from Kidston. **E** Contorted, heterogranular quartz-magnetite UST in chloritized monzonitic porphyry matrix from Ridgeway. The USTs seem to be fragmented during or shortly after their formation in a still viscous reacting magmatic matrix

we used for the identification of primary inclusions are those concentrated in growth zones perpendicular to the crystal growth direction or isolated, randomly distributed inclusions within the core of UST crystals (e.g., Roedder 1984). In addition to these structural characteristics, further evidence for primary origins of fluid inclusions are those that have a negative crystal or near negative crystal shape or a shape and orientation consistent with the growth direction of the crystal (Goldstein 2003). Pseudosecondary inclusions are inclusions that form along a healed fracture that develops and heals during the continued growth of the crystal.

Very few primary and secondary fluid inclusions are preserved in UST quartz of the two Bayan Uul samples. Most fluid inclusions in these samples are decrepitated. Rare melt inclusions contain a shrinking bubble and crystals in glassy matrix (Fig. 8a). The melt inclusions start to melt at 575 ± 25 °C and homogenize partially (glass + vapor) at 750 ± 25 °C (Table 3). Isolated pseudosecondary vapor-rich inclusions are common, and some of them form boiling assemblages with liquid-rich brine fluid inclusions with solid phases (Fig. 8b). The salinity of the fluid of the solid-bearing brine inclusions ranges between 18.3 and 23.1 wt.%. Younger generations of secondary fluid inclusions have decreasing salinities with decreasing homogenization temperatures that document episodes of fluid infiltration and overprinting of the UST.

The UST quartz of Oyu Tolgoi is intensively penetrated by different generations of fluids resulting in a dense network of fluid inclusion trails masking primary and pseudosecondary inclusions. Most of the inclusions are < 3 µm. Very few melt inclusions were found in crystal cores (Fig. 8c). These inclusions have an isomorph to euhedral shape and contain a vapor phase and crystals in a crystallized glass matrix. They start to melt at a temperature of 675 °C and homogenize partially (glass + vapor) at 825 °C.

Different generations of large fluid inclusions of 20 to 50 µm in diameter characterize the Oyut Ulaan UST quartz. Generally, two main inclusion assemblages can be

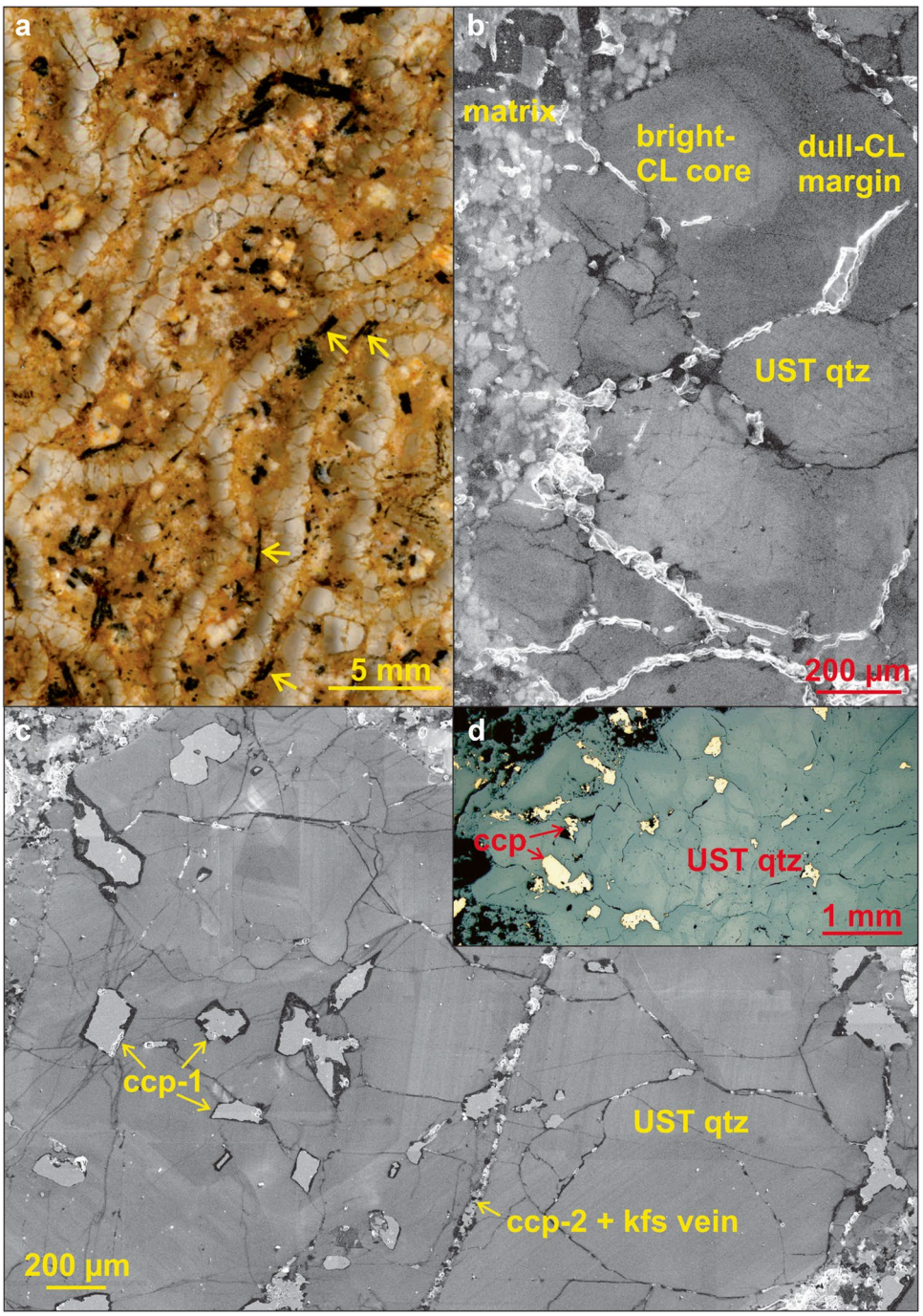

Fig. 5 Photomicrographs of textures observed in the Tsagaan Chuluut and Tampang UST samples. **a** Thin section scan illustrating the wormy, equigranular UST bands from Tsagaan Chuluut. The yellow arrows indicate example of amphibole phenocrysts of the porphyry matrix which are aligned parallel to the UST layer. **b** SEM-CL image of Tsagaan Chuluut UST quartz embedded in a fine-grained porphyry matrix seen on the upper edge of the image. The darker luminescent grain margins along some grain boundaries are interpreted as alteration structures rather than growth zoning. **c** SEM-CL of the Tampang UST quartz with fine, oscillatory growth zoning and euhedral to subhedral inclusions of chalcopyrite. **d** Optical microscopy reflected light image showing the high abundance of chalcopyrite inclusions (yellow) in UST quartz from Tampang

distinguished. The older and supposed primary fluid inclusion generation is characterized by heterogeneous trapping of solids, vapor, and liquid phase interpreted as a boiling assemblage. These liquid-rich inclusions start to melt at about 525 ± 25 °C and homogenize partially (glass + vapor) at 675 ± 25 °C. Secondary, CO_2-rich fluid inclusions are common. The fluid phase of this generation has 4.7–5.9 wt. % NaCl equivalent with T_h around 390 °C.

The UST quartz of Umnu Hutul contains rare melt inclusions in the core of crystals with a vapor phase in a glassy matrix (Fig. 8e). There are numerous round glassy inclusions containing crystalline solids, mainly topaz and mica. These inclusions start to melt at 525 ± 25 °C and homogenize partially (glass + vapor) at 675 ± 25 °C. Common are pseudosecondary fluid inclusions assemblages with various liquid/vapor ratios indicating boiling. Late aqueous fluid inclusions lacking vapor phase can be found along young healed microcracks.

In general, fluid inclusions are rare in the Tsagaan Chuluut UST quartz. There are a few small, (< 10 µm)

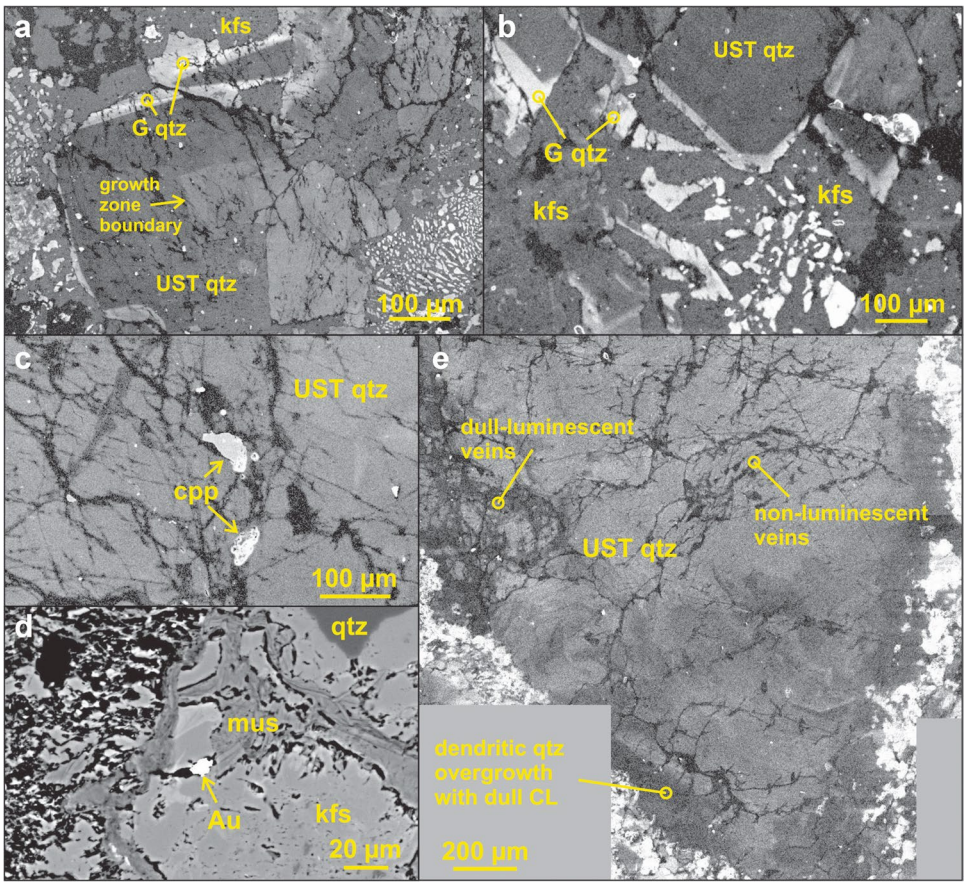

Fig. 6 Photomicrographs of textures observed in the Hada Sumu and Kidston UST samples. **a** SEM-CL image of dull luminescent Hada Sumu UST quartz with two growth zones and bright luminescent overgrowth of granophyric quartz. **b** SEM-CL image of granophyric K-feldspar-quartz intergrowth at the top of a UST crystal from Hada Sumu. **c** SEM-CL image of UST quartz from Kidston overprinted by different generations of healed fractures, one associated with chalcopyrite (ccp) mineralization. **d** BSE image showing native Au in the phyllic altered porphyry matrix of the Kidston sample. **e** SEM-CL image of the top of Kidston UST quartz crystals with dull luminescent alteration structures and an almost non-luminescent dendritic overgrowth

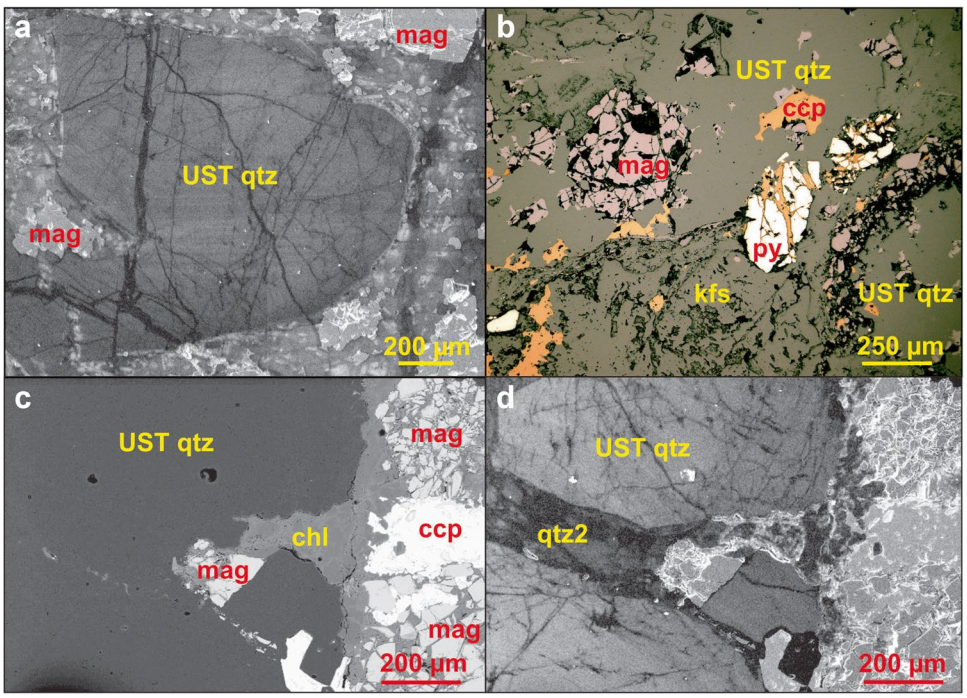

Fig. 7 Photomicrographs of textures observed in the Ridgeway sample. **a** SEM-CL image of UST quartz with fine, oscillatory growth zoning of low contrast cut by a network of thin, healed fractures healed with dull luminescent quartz. **B** Optical reflected light image illustrating the ore mineral sequence of crystallization magnetite (mag)-pyrite (py)-chalcopyrite(ccp). **c** BSE image of UST quartz cut by younger chlorite-bearing quartz (qtz2) vein (see also (**d**)). Fragmented magnetite crystals are embedded and partially replaced by a chlorite-chalcopyrite assemblage. **d** SEM-CL of the same area as shown (**c**)

pseudosecondary fluid inclusions with different portions of vapor phase indicating heterogeneous trapping. These fluid inclusions start to melt at about 675 ± 25 °C and homogenise partially at 775 ± 25 °C. Some fluid inclusions contain a second liquid phase, probably liquid CO_2, forming a meniscus between the vapor bubble and the aqueous

Table 3 Occurrence and microthermometic results of primary melt inclusions (MI) and primary and pseudosecondary fluid inclusions (FI) in UST quartz. Associations of vapor-rich and brine inclusions are interpreted as "boiling" assemblages. Due to the lack of workable inclusions, no Tm and Th were determined for the Ridgeway and Kidston samples. Ti-in-quartz thermo-barometer calculations are based on the assumed pressure of 1 kbar for all samples (see also Table 1). The provided Ti-in-quartz temperatures may represent minimum crystallization temperatures, except for sample Uyut Ulaan, due to uncertainties of the Ti saturation $a\mathrm{TiO_2}$. Assuming a minimum $a\mathrm{TiO_2}$ of 0.6 (see text for explanation), the Ti-in-quartz temperatures would be 47 to 81 °C higher

	Silicate MI	FI "boiling" assemblage	Multi-solid (brine) FI without co-trapped vapor FI	T_m (°C) of primary and pseudo-secondary inclusions ± 25 °C	T_h (°C) of primary inclusions ± 25 °C	Ti-in-quartz thermo-barometer acc. to Huang and Audétat (2012)
Bayan Uul	Y (P)	Y(PS)	-	575 (MI)	750 (MI)	702 ± 21
Oyu Tolgoi	Y (P)	-	-	675 (MI)	825 (MI)	774 ± 17
Oyut Ulaan	-	Y (P)	-	525 (FI)	675 (FI)	685 ± 34
Umnu Hutul	Y (P)	Y(PS)	-	525 (MI)	675 (MI)	588 ± 33
Tsagaan Chuluut	-	Y (PS)	-	675 (FI)	775 (FI)	746 ± 28
Tampang	Y (P)	-	-	775 (MI)	875 (MI)	680 ± 23
Hada Sumu	-	Y (PS)	-	525 (FI)	575 (FI)	628 ± 33
Kidston	-	-	-	-	-	643 ± 36
Ridgeway	-	-	Y (P)	-	-	638 ± 34

Tm, temperature of starting melting; *Th*, temperature of partial homogenization (silicate-glass + vapour phase); *Y*, yes, identified; *P*, primary inclusion; *PS*, pseudosecondary inclusion

phase. Late secondary fluid inclusions along trails are usually < 2 µm in diameter.

The UST quartz of Tampang contains glassy silicate melt inclusions with a shrinkage bubble and a solid phase (Fig. 8e). These melt inclusions start to melt at 775 ± 25 °C and homogenize partially at 875 ± 25 °C. Secondary CO_2 inclusions are common (one is shown in Fig. 8e) besides large secondary high-saline fluid inclusions with homogenization temperatures ranging between 223 and 324 °C.

The Hada Sumu UST quartz hosts common fluid inclusion assemblages of vapor-rich inclusions and liquid-rich brine inclusions, interpreted as heterogeneous trapping of a hyper-saline brine and vapor phase under boiling conditions (Fig. 8f). The inclusions start to melt at 525 ± 25 °C and homogenize partially (glass + vapor) at 575 ± 25 °C. The boiling assemblage is interpreted as pseudosecondary trapped inclusions. Secondary fluid inclusions with homogenization temperatures between 121 and 291 °C are very common. Most of them homogenize at 150 to 160 °C.

The UST quartz from Kidston is intensively overprinted by trails of secondary fluid inclusions; thus, intact primary fluid inclusions were not found. The few identified primary inclusions show features of palaeo-decrepitation. The temperature at which melting started of one early-stage, secondary brine inclusion with multiple solids was determined to be about 575 ± 25 °C.

In the UST quartz from *Ridgeway*, the primary fluid inclusion assemblages comprise euhedral magnetite crystals associated with a fluid and vapor phase and halite and other solids. Starting melting temperature and homogenization temperatures could not be determined. Because the magnetite microcrystals did not homogenize into the brine, they are most likely not part of the inclusion assemblage. The oldest generation of secondary fluid inclusions forms aqueous inclusions with a vapor phase and multiple crystalline phases. Recrystallized quartz in micro-shear zones contains tiny liquid-filled fluid inclusions with halite crystals. Vapor-rich fluid inclusions are rare. The youngest fluid inclusion generation consists of irregular liquid-filled fluid inclusions along healed cracks.

Trace elements of UST quartz and calculated quartz crystallization temperatures

Concentrations of Al and Ti in UST quartz determined by EPMA are plotted in Fig. 9 and listed in Table 4. Only UST quartz domains unaffected by signs of post-UST overprint, such as healed microcracks or diffusion rims, were analyzed. Highest average Ti concentrations were detected in UST quartz from Oyu Tolgoi and Tsagaan Chuluut with an average of 223 ± 28 and 184 ± 37 ppm, respectively (Fig. 9). The high values indicate high quartz crystallization temperatures (e.g., Huang and Audétat 2012), which are provided in Table 4 and summarized in Table 3.

The Ti activation ($a\mathrm{TiO_2}$) has to be known to estimate the crystallization temperatures of quartz when applying the Ti-in-quartz-geothermobarometer. For silica-rich melts, $a\mathrm{TiO_2}$ varies from 0.6 (rhyolitic melts) to 1 (dacitic melts) (e.g., Hayden and Watson 2007). Applying $a\mathrm{TiO_2}$ of 0.6 instead of 1 to our data would result in temperatures which are between 47 and 81 °C higher than the Ti-saturated temperatures. These Ti-undersaturated temperature estimates

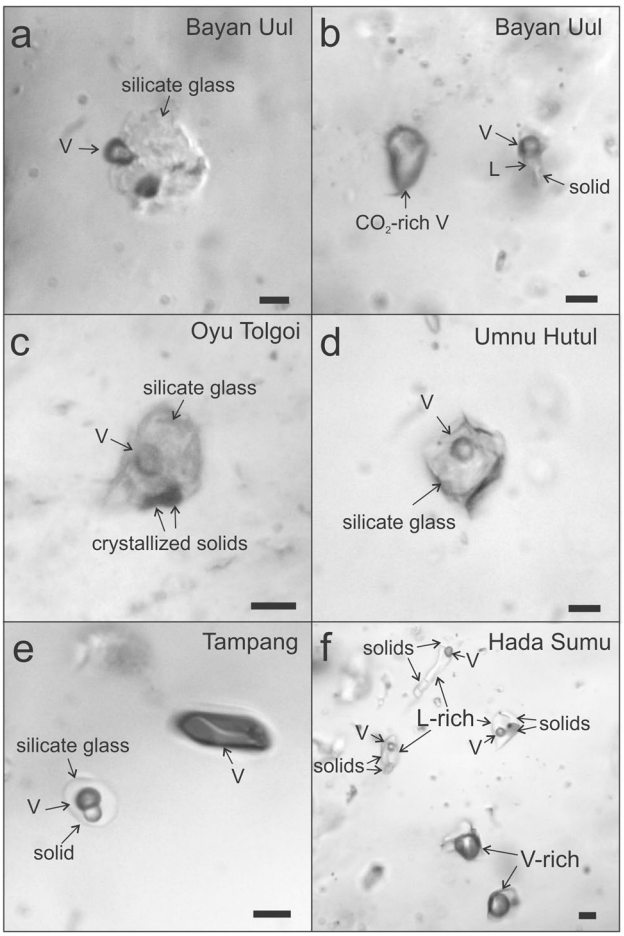

Fig. 8 Melt and fluid inclusions observed in UST quartz at room temperatures. **a** Melt inclusion consisting of a small vapor bubble and crystals in a crystallized silicate-glass matrix in the Bayan Uul sample. **b** Assemblage of secondary fluid inclusions with different liquid/vapor phase ratios indicating boiling observed in the Bayan Uul. **c** Melt inclusion containing a volatile phase (V) and two solid phases hosted by Oyu Tolgoi UST quartz. **d** Glassy melt inclusion with vapor phase in the Umnu Hutul sample. **e** Silicate glass inclusion with vapor bubble and a crystal (solid) in UST quartz from Tampang. On the right is a CO_2 inclusion. **f** Assemblage of fluid inclusions with different liquid/vapor phase ratio and halite crystals in the Hada Sumu UST quartz interpreted as boiling assemblage of a saturated solution. Scale bars = 5 µm

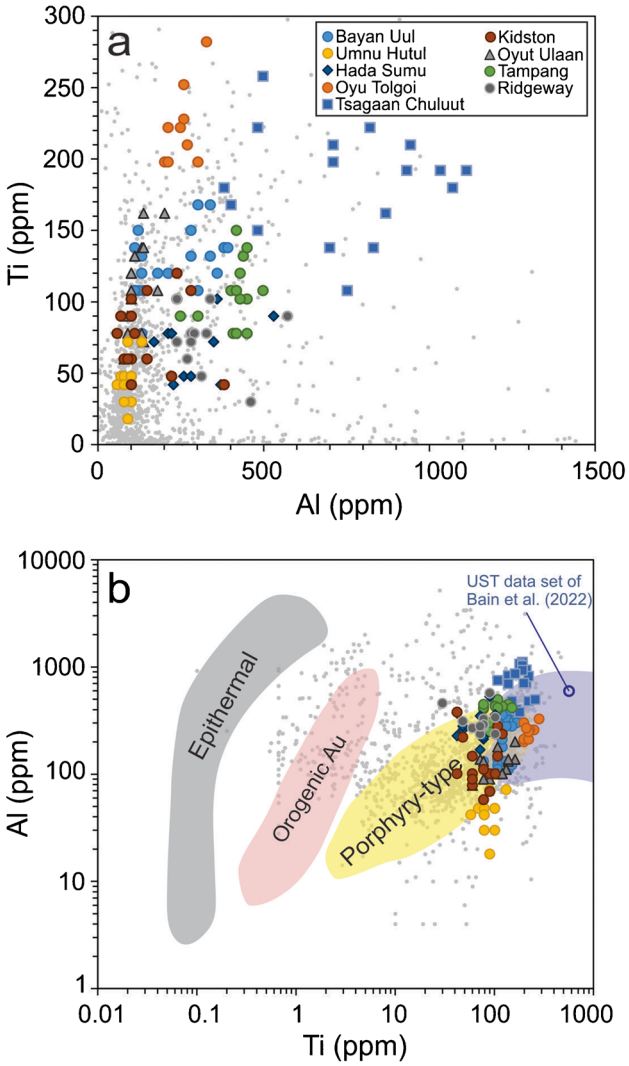

Fig. 9 **a** Al versus Ti concentration plot of the investigated UST quartz samples. The small grey dots represent quartz data of porphyry A- to E-type vein quartz by Landtwing and Pettke (2005), Rusk et al. (2008), Müller et al. (2010), Tanner et al. (2013), Bennett (2014), Maydagán et al. (2015), Rottier (2016), Mao et al. (2017), Tsuruoka (2017), Cernuschi et al. (2018), Rottier et al. (2018), and Carter and Williamson (2022). The Ti and Al concentrations of UST quartz from this study overlap with the highest Ti and Al values determined for the stockwork/vein quartz from these previous studies. **b** Logarithmic Ti versus Al discrimination plot of epithermal, orogenic Au and porphyry quartz according to Rusk (2012). The violet-shaded field corresponds to the low-Ti end of the UST quartz data from Saginaw Hill, Arizona, USA by Bain et al. (2022). The small grey dots represent the same set of published data shown in (**a**)

appear unrealistically high for most of the studied systems, particularly when compared to the determined homogenization temperatures of primary inclusions in the UST quartz (Table 3). In previous publications on the application of the Ti-in-quartz-geothermobarometer to porphyry systems, it has been shown that porphyry melts are commonly rutile-saturated (e.g., Müller et al. 2010). It is of course debatable that the directly porphyry-melt-derived fluids from which the UST crystallized (within the porphyry melt) were saturated in Ti as well. In the sample from Oyut Ulaan, rutile is part of the UST assemblages (Table 2), and Ti saturation is evident in that particular case. Thus, we indicated the calculated temperatures provided in Tables 3 and 4 as minimum crystallization temperatures of quartz considering possible uncertainties of the $aTiO_2$.

UST quartz from Bayan Uul, Oyut Ulaan, and Tampang has moderately high Ti of 128 ± 22, 113 ± 31, and 106 ± 22 ppm, respectively. Moderate Ti was detected in UST quartz from Kidston, Hada Sumu, and Ridgeway with

Table 4 Aluminum and Ti concentrations (in ppm) of UST quartz determined with EPMA. Temp.: Calculated UST quartz crystallization temperature (in °C) applying the Ti-in-quartz thermobarometer by Huang and Audétat (2012). Ti-in-quartz thermo-barometer calculations are based on the assumed pressure of 1 kbar for all samples. The provided Ti-in-quartz temperatures may represent minimum crystallization temperatures, for except sample Uyut Ulaan, due to uncertainties of the Ti saturation $a\mathrm{TiO_2}$. Assuming a minimum $a\mathrm{TiO_2}$ of 0.6 (see text for explanation), the Ti-in-quartz temperatures would be 47 to 81 °C higher

Sample	Al	Ti	Temp	Sample	Al	Ti	Temp	Sample	Al	Ti	Temp
Bayan Uul tur	138	108	683	Oyut Ulaan	101	120	696	Tampang	418	78	647
Bayan Uul tur	122	108	683	Average	122	113	685	Tampang	450	78	647
Bayan Uul tur	132	120	696	STDV	33	31	34	Average	412	106	680
Bayan Uulkfs	339	168	737	Umnu Hutul	132	72	639	STDV	61	22	23
Bayan Uulkfs	302	168	737	Umnu Hutul	79	42	586	Hada Sumu	349	72	639
Bayan Uulkfs	281	150	723	Umnu Hutul	79	42	586	Hada Sumu	360	102	677
Bayan Uulkfs	111	138	712	Umnu Hutul	101	30	556	Hada Sumu	169	72	639
Bayan Uulkfs	132	132	707	Umnu Hutul	69	48	598	Hada Sumu	212	78	647
Bayan Uulkfs	122	150	723	Umnu Hutul	101	48	598	Hada Sumu	222	78	647
Bayan Uulkfs	381	138	712	Umnu Hutul	58	42	586	Hada Sumu	259	48	598
Bayan Uulkfs	180	120	696	Umnu Hutul	79	30	556	Hada Sumu	371	42	586
Bayan Uulkfs	132	78	647	Umnu Hutul	90	72	639	Hada Sumu	530	90	663
Bayan Uulkfs	111	108	683	Umnu Hutul	79	48	598	Hada Sumu	228	42	586
Bayan Uulkfs	111	108	683	Umnu Hutul	101	48	598	Hada Sumu	281	48	598
Bayan Uulkfs	381	138	712	Umnu Hutul	79	42	586	Average	298	67	628
Bayan Uulkfs	212	120	696	Umnu Hutul	90	18	514	STDV	107	21	33
Bayan Uulkfs	281	132	707	Average	87	45	588	Kidston	381	42	586
Bayan Uulkfs	339	132	707	STDV	19	15	33	Kidston	101	60	620
Bayan Uulkfs	392	138	712	Tsagaan Chuluut	402	168	737	Kidston	148	108	683
Bayan Uulkfs	302	108	683	Tsagaan Chuluut	752	108	683	Kidston	101	90	663
Bayan Uulkfs	360	120	696	Tsagaan Chuluut	482	222	774	Kidston	111	78	647
Average	231	128	702	Tsagaan Chuluut	831	138	712	Kidston	101	102	677
STDV	108	22	21	Tsagaan Chuluut	699	138	712	Kidston	58	78	647
Oyu Tolgoi	201	198	759	Tsagaan Chuluut	710	210	766	Kidston	69	90	663
Oyu Tolgoi	259	252	792	Tsagaan Chuluut	381	180	746	Kidston	79	60	620
Oyu Tolgoi	302	198	759	Tsagaan Chuluut	943	210	766	Kidston	101	42	586
Oyu Tolgoi	259	228	778	Tsagaan Chuluut	1112	192	754	Kidston	90	60	620
Oyu Tolgoi	212	198	759	Tsagaan Chuluut	821	222	774	Kidston	148	60	620
Oyu Tolgoi	212	222	774	Tsagaan Chuluut	1070	180	746	Kidston	238	120	696
Oyu Tolgoi	249	222	774	Tsagaan Chuluut	498	258	795	Kidston	222	48	598
Oyu Tolgoi	328	282	808	Tsagaan Chuluut	1033	192	754	Kidston	238	102	677
Oyu Tolgoi	270	210	766	Tsagaan Chuluut	932	192	754	Kidston	281	108	683
Average	255	223	774	Tsagaan Chuluut	482	150	723	Average	154	78	643
STDV	42	28	17	Tsagaan Chuluut	710	198	759	STDV	92	26	36
Oyut Ulaan	90	90	663	Tsagaan Chuluut	868	162	732	Ridgeway	281	78	647
Oyut Ulaan	90	78	647	Average	749	184	746	Ridgeway	238	102	677
Oyut Ulaan	132	138	712	STDV	234	37	28	Ridgeway	281	78	647
Oyut Ulaan	201	162	732	Tampang	450	102	677	Ridgeway	328	78	647
Oyut Ulaan	138	162	732	Tampang	418	108	683	Ridgeway	270	60	620
Oyut Ulaan	180	108	683	Tampang	439	132	707	Ridgeway	238	72	639
Oyut Ulaan	111	132	707	Tampang	450	138	712	Ridgeway	572	90	663
Oyut Ulaan	111	132	707	Tampang	408	78	647	Ridgeway	291	78	647
Oyut Ulaan	138	72	639	Tampang	249	90	663	Ridgeway	312	48	598
Oyut Ulaan	101	102	677	Tampang	418	150	723	Ridgeway	281	72	639
Oyut Ulaan	79	60	620	Tampang	429	120	696	Ridgeway	461	30	556
Oyut Ulaan	132	78	647	Tampang	302	90	663	Ridgeway	339	102	677

Table 4 (continued)

Sample	Al	Ti	Temp	Sample	Al	Ti	Temp	Sample	Al	Ti	Temp
Oyut Ulaan	101	108	683	Tampang	498	108	683	Average	324	74	638
Oyut Ulaan	138	138	712	Tampang	402	108	683	STDV	98	21	34
Oyut Ulaan	101	120	696	Tampang	429	102	677				

average concentrations of 78 ± 26, 67 ± 21, and 74 ± 21 ppm, respectively. Quartz from Umnu Hutul has the lowest Ti of 45 ± 15 ppm.

The Al concentration of the UST quartz falls into three groups. Very high Al with an average of 749 ± 234 ppm is observed in the quartz from Tsagaan Chuluut. Aluminum contents of the second group including Oyu Tolgoi, Hada Sumu, Bayan Uul, and Ridgeway range from 250 to 440 ppm. Samples of the third group comprising Oyut Ulaan, Umnu Hutul, and Kidston have low average concentrations of about 90 to 150 ppm.

In most cases, calculated quartz crystallization temperatures overlap with homogenization temperatures of primary inclusions, except for the Tampang and Hada Sumu quartz where calculated temperatures are significantly higher as the homogenization temperatures. Compared to previously published trace element data of A- to E-type vein quartz in porphyry systems (Landtwing and Pettke 2005; Rusk et al. 2008; Müller et al. 2010; Tanner et al. 2013; Bennett 2014; Maydagán et al. 2015; Rottier 2016; Mao et al. 2017; Tsuruoka 2017; Cernuschi et al. 2018; Rottier et al. 2018; Carter and Williamson 2022), our data plot at the high Ti end of the porphyry field defined by Rusk (2012; Fig. 9b). Our data overlap just with the lowest Ti concentrations of UST quartz from the Saginaw Hill porphyry in Arizona published by Bain et al. (2022). Some of the Ti concentrations determined by Bain et al. (2022) on UST quartz, ranging up to 12,369 ppm, appear unrealistically high for natural quartz considering published data on porphyry quartz. Thus, the investigated UST quartz represents the hottest and thus earliest quartz generation of the porphyry mineralization sequence precipitated after the igneous quartz of the porphyry host.

Discussion

An attempt to classify USTs in porphyry systems

The overall structural appearance and spatial setting of the investigated USTs in porphyry systems are similar (Figs. 1 and 4). Crystal size, layer shape, and number of UST sequences show a great variety. The implication of all investigated porphyry-hosted USTs is that quartz crystals nucleated along subparallel mineralogical and/or geochemical interfaces in the apical part of stock-like porphyry intrusions. The layered sequences occur at or close to the upper horizontal intrusion contact, at porphyry sub-intrusion contacts, and sometimes below a massive silica cap (Fig. 2). The quartz crystals of each UST layer grew more or less in the same direction pointing inward away from the walls of the intrusion. The c axis of the quartz crystals is typically at a high angle to the nucleation interface plane. In general, the aligned crystals appear planar on the side of the nucleation interface and have euhedral quartz terminations on the other.

However, in detail, each UST locality has its own specific structural features controlled by local conditions (Figs. 1, 3, 4, 5, 6, and 7). Figure 10 a textural classification of macro (hand specimen) scale USTs observed in our samples is proposed. The classification broadly distinguishes two major groups, equigranular and heterogranular USTs which are subdivided according to the UST layer structure into straight (Fig. 10a and d), wavy (Fig. 10b and e), or contorted/brain-like types (Fig. 10c and f). In addition, there is the group of disturbed USTs which comprise incompletely developed UST layers (Fig. 10g) and ductile- (Fig. 10h) or brittle-fragmented (Fig. 10i) UST sequences. Ductile fragmentation is due to movement of the un-consolidated melt matrix (magma flow). Brecciated USTs develop when the sequence underwent brittle fragmentation after solidification. The structures of the third group may occur in combination with or superimpose those of the equi- and heterogranular groups. A complementary classification of principle types of growth textures and shapes of individual UST quartz crystals within a single UST layer is illustrated in Fig. 11: equigranular UST layers comprising elongated quartz crystals (Fig. 11a), heterogranular UST layers comprising elongated quartz crystals (Fig. 11b), equigranular UST layers of isometric quartz crystals (Fig. 11c), and heterogranular quartz UST layers with feldspar micro-UST within quartz crystals along growth zone boundaries (Fig. 11d).

Straight, equigranular quartz UST layers are developed in the samples from the Umnu Hutul W–Mo porphyry and Oyut Ulaan Cu–Mo–Au porphyry corresponding to the structural type in Fig. 10a. These are the most silica-rich and fractionated porphyry magmas, which are indicated not only by the high quartz content and the aplitic, topaz-bearing (in

the case of Umnu Hutul) matrix (Table 2) but also reflected in the relatively low to moderate crystallization temperatures of 588 ± 33 and 685 ± 34 °C, respectively (Table 3). The large Oyut Ulaan quartz crystals exhibit thin layers of tiny K-feldspar crystals forming micro-USTs within the UST quartz along growth zone boundaries (Fig. 1d) representing the UST crystal type illustrated in Fig. 11d. This type has also been reported from the W–Mo mineralized Sannae-Eonyang granite in South Korea (Seo et al. 2021), the Logtung W–Mo deposit in the Yukon Territory, Canada (Lowenstern and Sinclair 1996), and the Tate River Sn prospect in North Queensland, Australia (Kirwin 2006), implying that this texture represents a distinct genetic type of UST.

Samples from Hada Sumu (Fig. 4b and c) and Ridgeway (Fig. 4e) comprise heterogranular wavy comb quartz layers. The layering in these samples is not as regular-cyclic as the planar examples of Umnu Hutul and Oyut Ulaan. The schematized structure of this UST type is shown in Fig. 10e. In the case of Hada Sumu, the comb quartz bands alternate with layers of co-genetic, micro-granophyric K-feldspar-quartz intergrowths, whereas the Ridgeway USTs are in a porphyry matrix. In the Ridgeway sample, some quartz layers are not completely developed, meaning that the layers (nucleation interfaces) are not entirely occupied by quartz crystals and the quartz crystals have variable sizes along the same layer. This UST layer type is simplified in Fig. 11b.

Equigranular, contorted, and brain-like USTs (Fig. 10c) with relatively small (< 2 cm) crystal sizes are most common in the investigated porphyries. Contorted UST layers are developed within a phenocryst-rich, porphyry matrix. Most strongly contorted brain textures are developed in the samples from Oyu Tolgoi and Tampang porphyries (Figs. 1c and 4a). In these cases, parts of USTs became ductile fragmented due to magma flow of the porphyry host melt, as schematically illustrated in Fig. 10h. Samples from Bayan Uul, Tsagaan Chuluut, and Kidston have more regular brain textures transitional to wavy USTs with the elongated quartz crystals of relative consistent size along one layer (Figs. 1a, 1b, 1f, and 4d). At Tsagaan Chuluut, the UST quartz crystals are more or less isometric and have consistent crystal size corresponding to the type in Fig. 11c. Samples with brain textures have generally higher crystallization temperatures (about 640 to 770 °C) than USTs of more regular structures (about 590 to 680 °C) (Table 3). UST quartz of contorted layers shows commonly primary growth zoning in CL (Figs. 3c, 3e, and 5c).

Implications for UST genesis in porphyry systems

In the studied cases, quartz UST crystallization represents the first transitional magmatic-hydrothermal crystallization stage in a series of kinematic and dynamic processes in porphyry systems, which can further evolve to form sheeted and stockwork quartz veins, disseminated mineralization, and breccia pipes. The postulated early stage of the magmatic-hydrothermal transition recorded by the UST is confirmed by the detected high crystallization temperatures in the range of 575 to 875 °C documented by the homogenization temperatures of primary and pseudosecondary inclusions and Ti-in-quartz geothermobarometry of the UST quartz (Table 3). Considering the Ti-in-quartz-based calculations only, the crystallization temperatures of UST quartz are between 590 and 770 °C. These temperatures overlap with the solidus temperatures of the porphyry host melts (e.g., Yang and Bodnar 1994) and are, on average, higher than estimates of porphyry mineralization from about 350 to 700 °C (Seedorff et al. 2005; Sillitoe 2010; Bodnar et al. 2014; Bain et al. 2022). Temperatures for UST formation of about 650 °C have been described by Bain et al. (2022) from the Saginaw Hill porphyry in AZ, USA, which is consistent with our early-stage UST temperatures.

Based on textural observations, we conclude that the condition of the porphyry host melt (size, distribution, and proportion of phenocrysts in the melt, solidification degree of the melt) affects the development and, thus, the resulting shape of the UST layers. Most of the investigated USTs likely crystallized in a crystal mush (Bayan Uul, Oyu Tolgoi, Tsagaan Chuluut, Kidston, Tampang, and Ridgeway; e.g., Fig. 5a). Others probably crystallized coevally with an aplitic melt phase (Umnu Hutul, Fig. 1e) as indicated by such textures or a melt phase forming micro-granophyric or feldspar micro-USTs (Hada Sumu and Oyut Ulaan, Figs. 1d, 4b, and c). In general, in a co-genetic aplite matrix, UST bands are more planar than in phenocryst-rich mush.

In principle, there are two well-established, previously published models for UST sequence formation: the open-system and closed-system models. These are summarized below and then compared and contrasted to our model, which is introduced at the end of this chapter.

Closed-system model for UST formation

London (2009, 2014) explained UST formation in granitic pegmatites (megacrystic layers of quartz, feldspar, mica, and/or tourmaline etc., alternating with aplite) as a self-evolving closed-system process that is kinetically driven and dominated by the effects of liquidus undercooling. The USTs result mostly from the accumulation of fluxes in the melt that enhance the diffusion of Al and Si. Those fluxes are likely to become enriched in a boundary-layer liquid that forms at the growth front of crystal layers, i.e., UST. The crystal nuclei preferentially form at a solid/melt interface and start to grow oriented toward the inner parts. The crystal growth rate is much higher than the nucleation rate due to high H_2O contents in the surrounding melt (London 2014). The growth of coarse crystals is explained by the accumulation

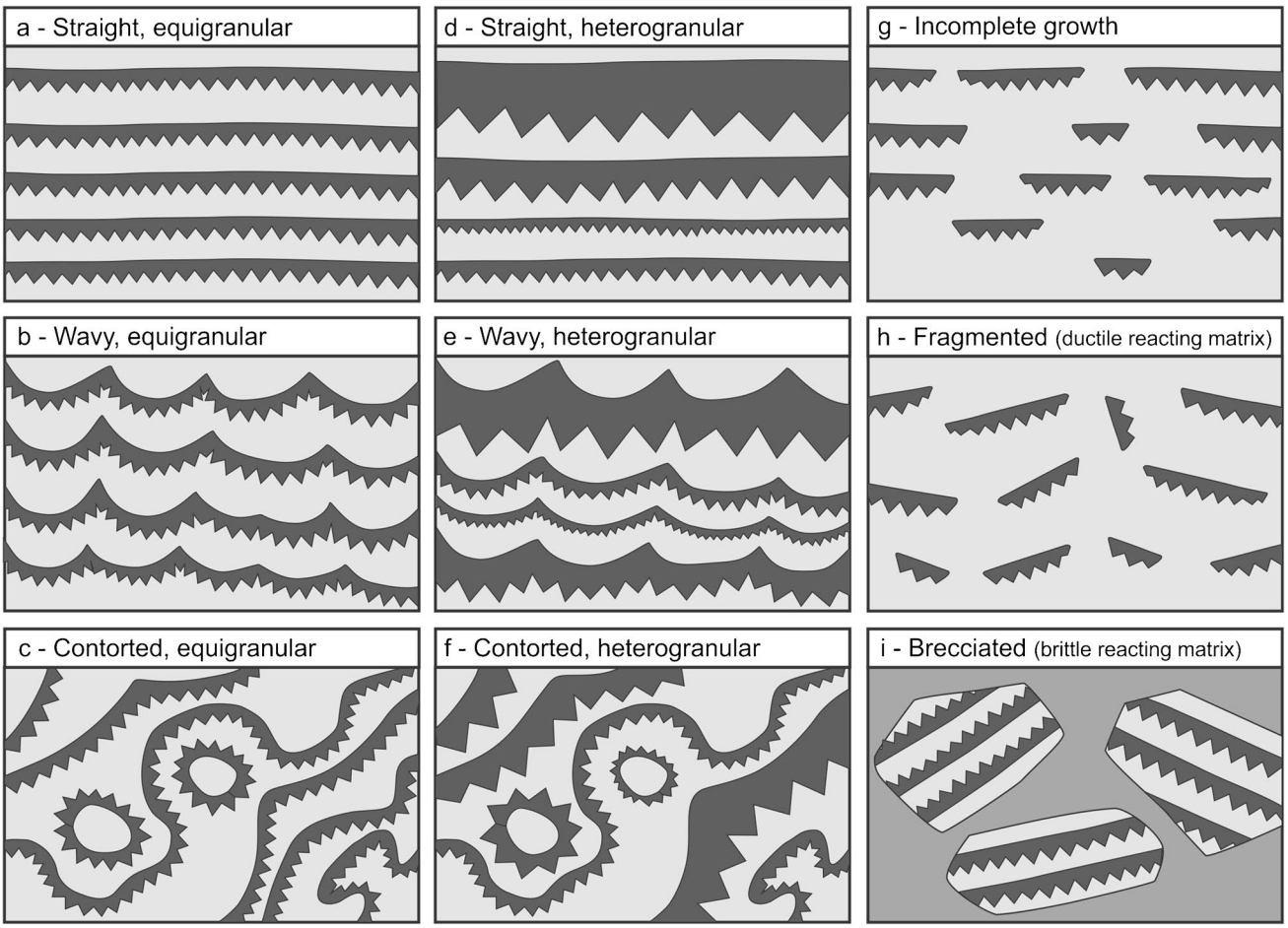

Fig. 10 Textural types of UST layer sequences observed in porphyry and intrusion-related Au deposits from this study. Textures (**a**) to (**f**), schematizing equigranular and heterogranular straight, and wavy and contorted structures, should be considered textural end members and there are transitions between the end members. The right column represents specific conditions (**g** insufficient or disrupted SiO_2 supply during quartz UST growth, **h** matrix melt movement during UST crystallization, and **i** brecciation after UST solidification), which affected or overprinted UST formation

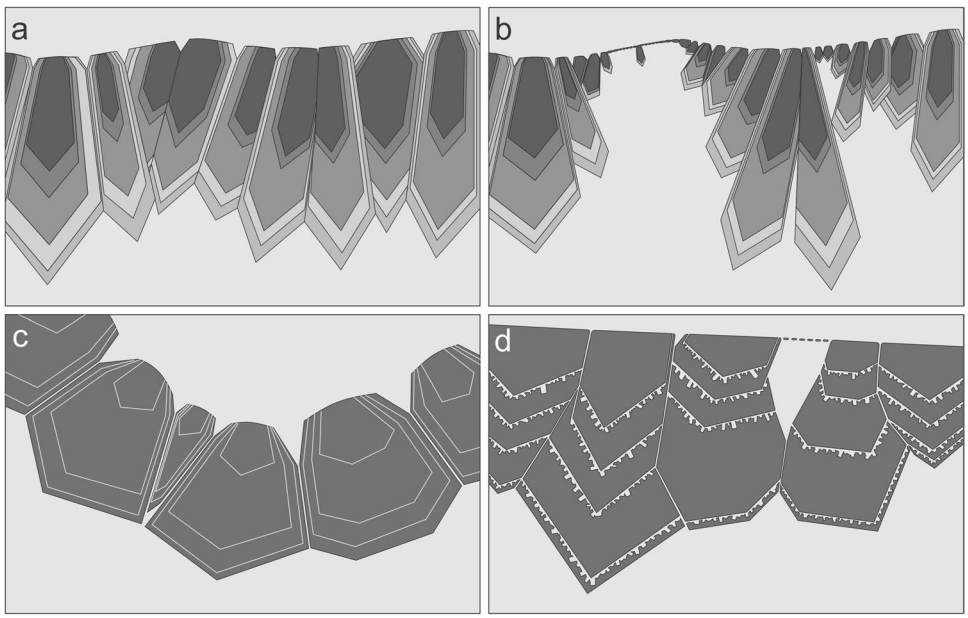

Fig. 11 Principle types of growth textures and shapes of UST quartz crystals observed in the investigated samples. **a** Equigranular UST layer comprising elongated quartz crystals with high-contrast CL-visualized growth zoning. **b** Heterogranular UST layer comprising elongated quartz crystals with high-contrast CL-visualized growth zoning. **c** Equigranular UST layer of isometric quartz crystals with low-contrast CL-visualized growth zoning. **d** Heterogranular quartz UST layer with feldspar micro-UST within quartz crystals along growth zone boundaries

of fluxing elements in a boundary layer that follows the temperature gradient. The fluxes lower the viscosity of the layer; thus, diffusion and rapid crystal growth are facilitated (London 2009). If the growth rate takes over the diffusion rate of mineral-building ions in the surrounding melt, the crystallization of the UST layer stops and aplite formation becomes the dominant process. This pegmatite UST model can be well applied for aplite-hosted USTs of silica-rich, fractionated melt systems such as the Umnu Hutul W–Mo porphyry. The monzogranite-hosted Timbarra Au deposit in New South Wales, Australia is another example of an interpreted closed-system quartz UST sequence (Mustard 2001). However, the monomineralic quartz UST typically hosted by porphyry melt mush without an obvious co-genetic aplite phase may require an adjustment of the UST model established for pegmatites.

Open-system model for UST formation

In contrast to the closed system model (London 2009), Shannon et al. (1982), Kirkham and Sinclair (1988), Lowenstern and Sinclair (1996), Kirwin (2005), Carter and Williamson (2022), and Bain et al. (2022) suggested that a pressure rise and drop sequence is the most probable path to supercooling and crystallization leading to the formation of multiple USTs (Fig. 12a to d). The initial over-pressuring is assumed to be related to the exsolution of the magmatic fluid or melt as the porphyry melt becomes oversaturated in H_2O and other fluxes. In shallow porphyry intrusions, the H_2O saturation is mainly achieved through cooling. Crystallization of water-free mineral phases contributes to the saturation as well. The exsolution is associated with a significant pressure increase in the crystallizing porphyry system (e.g., Halls 1994), which may lead to a sudden opening of the system followed by rapid decrease in pressure. The first comb quartz layer crystallizes at the top of the porphyry stock from the exsolved magmatic fluid (Fig. 12a and b). After the system is sealed, exsolved magmatic fluid together with exsolved vapor is fed to the cupola by degassing and over-pressure may build up again leading to the next system opening (Fig. 12c and d). Periodic opening of the system appears plausible, particularly for irregular UST (Fig. 10d, e, and f). However, veining (hydrofracturing due to hydraulic collapse) and brecciation representing depressurization events seem to postdate the UST formation in all investigated cases. So far, field observations that link sub-horizontal UST quartz layers directly to early-stage A veins (according to the definition of Gustafson and Hunt 1975) are lacking. Even this scenario has not been observed. Lowenstern and Sinclair (1996) postulated this theoretical setting, which is shown in Fig. 12b to d. Moreover, the formation of cyclic nucleation interfaces with consistent thickness of melt and UST quartz crystal layers, as observed at Umnu Hutul, Bayan Uul, Tsagaan Chuluut, and Kidston, is challenging to explain by multiple and forceful reopening of the system without affecting existing UST layers. Similar thickness and distance of comb quartz layers would imply that each growth stage crystallized approximately from the same amount of melt or fluid and/or that the system opens at consistent time intervals.

Integration of our results with existing models

In four of ten investigated UST quartz samples (Bayan Uul, Oyu Tolgoi, Umnu Hutul, and Tampang), silicate melt inclusions that were identified primarily in the core of UST crystals (Table 3) are evidence for initial crystallization from a silica-rich melt. The trapped melt is enriched in water as indicated by 10–20 vol.% large volatile bubbles in melt inclusions and in fluxes such as F as indicated by the topaz microcrystals found in the melt inclusions of the Umnu Hutul UST quartz, for example. Bain et al. (2022) detected up to 0.3wt.% B and 3.8 wt.% P_2O_5 in similar melt inclusions from the core of UST quartz crystals in the Saginaw Hill porphyry, confirming the common flux enrichment of melts that initiate UST crystallization. Flux enrichment serves to increase quartz and water solubility and lowers the viscosity of such melts (e.g., Dingwell 1988), allowing the melt to migrate easily through the crystal mush. These flux-rich melts would separate from the solidifying porphyry melt and build up in traps of the porphyry cupola at the site of UST formation (Kirwin 2005). The process of separation of flux-rich melts from porphyry melts has been documented (e.g., Bain et al. 2022). However, the following melt-fluid separation and its effect on the formation of UST sequences are less well understood. The melt and fluid inclusions in four of our samples show no evidence of fluid separation during the early growth stage (core) of UST quartz crystals. However, in five of our samples, fluid inclusion boiling assemblages were observed in the core of crystals (Oyut Ulaan) or at crystal margins (Bayan Uul, Umnu Hutul, Tsagaan Chuluut, and Hada Sumu) documenting early melt-fluid separation. In the case of Oyut Ulaan, the assemblage is interpreted as primary and in the other cases as pseudosecondary (Table 3). The "boiling assemblage" is indicative of fluid-vapor separation (Hedenquist et al. 1998; Koděra et al. 2018; Mernagh and Mavrogenes 2019), which occurred during the stage of UST crystallization when the assemblage was trapped in quartz. The primary nature of the "boiling" assemblage identified in the Oyut Ulaan quartz implies that the UST formed during brine-vapor phase separation when the porphyry system opened, releasing mineralizing fluids. This observation is also confirmed by the mineral paragenesis that suggests that Cu mineralization is co-genetic with the UST quartz

(Table 2). The Ridgeway UST quartz is the only sample in which brine inclusions without coeval vapor-rich inclusions were identified as primary inclusions (Table 3). In this case, the lack of coeval vapor-rich inclusions may be interpreted either in the way that the magmatic-hydrothermal fluid may have exsolved as a single-phase brine or that the vapor phase might have escaped prior to trapping. The first case might be possible since pressure and temperature conditions (< 1 kbar and about 640 °C; see Tables 1 and 3) and moderate brine salinities place the Ridgeway system at the boundary of the single liquid phase/liquid–vapor immiscibility field (e.g., Bodnar and Vityk 1995). However, it is also possible that the vapor phase had left the system before UST formation. The observed magnetite microcrystals associated with the brine inclusions, which do not homogenize with the brine, were presumably adhered to passing brines as they precipitate, followed by buoyant segregation and rise of the magnetite suspension toward the intrusion cupola as described by Knipping et al. (2015). The buoyancy-driven rise of the magnetite-transporting brines is, however, not necessarily associated with a depressurization-caused brine-vapor separation (Knipping et al. 2015). In summary, the data obtained for the Ridgeway sample are not entirely conclusive, but it is likely that the UST sequences formed after brine-vapor separation.

The results for other samples from the study area can be interpreted in two ways. First, in the way of the open-system

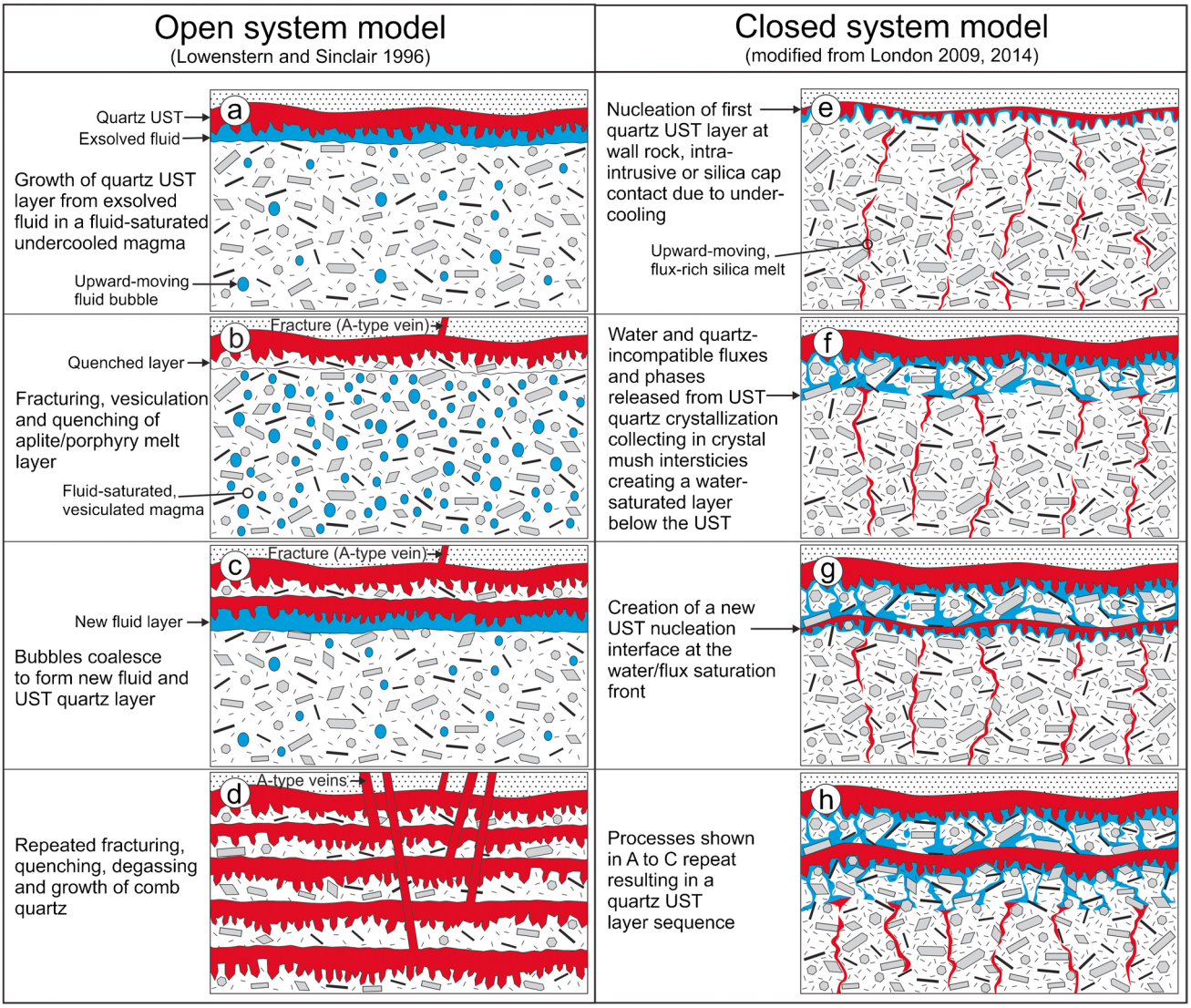

Fig. 12 Schematic open-system (**a** to **d**) and closed-system models (**e** to **h**) for the formation of UST sequences in the cupola of some Au–Cu porphyries. The primary difference between the two models is that in the open system exsolved fluids are periodically released after the formation of each individual UST layer, whereas in the closed system the exsolved fluids are trapped as long the UST sequence forms. See text for additional discussion

model of cyclic depressurization, each UST layer presents a sudden pressure drop (Fig. 12a–d) or, alternatively, the UST forms as a result of boundary layer processes prior to system opening similar to the model by London (2009, 2014). The pressure drop, the fundamental process of the open-system model, causes the magmatic fluid to undergo phase separation into coexisting hypersaline brine and vapor (e.g., Heinrich et al. 1999) documented by fluid inclusion assemblages of a brine and vapor-rich phase trapped in the growing UST quartz. This scenario could be applicable to the Oyut Ulaan UST sequence because in this sample, the fluid boiling assemblages are interpreted as primary trapped fluids. However, the pseudosecondary setting of the boiling assemblage in the Bayan Uul, Umnu Hutul, Tsagaan Chuluut, and Hada Sumu samples is more challenging to explain by this model, particularly for those samples that contain primary melt inclusions (Bayan Uul, Umnu Hutul, and Tsagaan Chuluut). In these samples, UST crystallization started from a silica melt prior to phase separation and, thus, prior to pressure drops. Because of the not documented pressure drop, a modified closed-system model, which in principle bases on processes postulated by London (2009, 2014), might be applied to these localities as explained in the following and illustrated in Fig. 12e to h. The UST formation was coeval with the crystallization of the porphyry host melt as documented by the alignment of shape-anisotropic crystals parallel to the UST layers (e.g., Fig. 5a). This observation implies that the porphyry melt was not completely crystallized and reacted as a dense crystal mush, allowing the formation of nucleation interfaces where the UST layer crystallized either immediately below the upper contact to the wall rock due to undercooling or at a stock-internal contact of two porphyry phases (Fig. 12e). Kirwin (2005) described cases where UST formed immediately below massive silica caps. We suggest that during the UST quartz crystallization, water and other quartz-incompatible phases are released and they accumulate in crystal mush interstices in front of (below) the growing UST layer (Fig. 12f). The crystallizing quartz crystal layer reacts as a sealing carapace so that the released water is not able to rise upward and, thus, cannot leave the system. The water and quartz-incompatible phases continuously fill the interstices in the crystal mush, and at one point, the interstitial water layer hinders the supply of silica for continuous quartz growth and crystal growth stops. The water-rich melt, however, is continuously fed into the water-saturated crystal mush layer and new quartz nucleation interfaces form and the UST layer formation repeats (Fig. 12c and d). This process continues until either the system opens due to hydraulic collapse or the system runs out of volatiles. The accumulated phases between the UST layers remain stationary, react with the surrounding matrix to some extent, and/or are drained when the system opens.

Nonetheless, the pseudosecondary setting of the "boiling" assemblages identified in a number of investigated samples could be trapped before a new UST layer was formed; in that case, the open-system model would apply, and alternatively if the "boiling" event superimposed the entire UST sequence after its formation than the closed-system model would predominantly apply. Thus, our data are not entirely conclusive except for the Oyut Ulaan and Ridgeway localities, which formed during brine-vapor separation in an open-system setting. The Ridgeway sample has the most heterogeneous UST in terms of crystal size variation, layer irregularity, and sequence fragmentation (Fig. 4e), which verifies crystallization in a disrupting open-system setting. The UST from Oyut Ulaan is characterized by K-feldspar micro-UST alternating with growth zones of megacrystic UST quartz (Figs. 1d and 11d). Open-system growth of this type of UST texture (Fig. 11d) might be indicative for open-system formation as suggested previously by Lowenstern and Sinclair (1996) and Seo et al. (2021). In summary, the described UST sequences from nine Asian and Australian porphyry and intrusion-related Au deposits and prospects are texturally diverse looking at detail and, despite similar overall appearance and spatial setting, maybe does not allow a common explanation for formation of quartz UST sequences.

The question remains to be which parameters control the evolution of a massive silica cap prior to UST layer sequence precipitation. Silica caps occur at the exo-contact of porphyry stocks with direct contact to the overlaying host rocks. Similar to the UST sequences, they are interpreted as quartz crystallization from over-pressured melts (Kirwin 2005). From field observations, it is evident that the silica cap cooling front migrated downward from contact and sealed the system for fluids arriving from below and UST would start to form. This scenario is exposed, for example, at the Zuun Mod Mo–Cu porphyry in South Gobi, Mongolia where massive silica bodies at the top contact of the porphyry stock are seen to transition over several meters directly into quartz UST layers (Kirwin 2005).

UST as vector for Cu–Au exploration in porphyry systems

Six out of ten investigated UST samples contain very high Au contents (Table 1). In the samples from Kidston and Tampang, native Au grains of about 10 µm were identified (Fig. 6d). The mineralogy, textural and paragenetic relationships, and alteration sequences revealed, however, that in all cases the Au enrichment postdates the UST formation. At Oyut Ulaan and Tampang, the UST quartz formation is co-genetic with Cu–Fe sulfide mineralization (Fig. 5c and d), whereas in the other localities the UST formation predates sulfide mineralization. Planar, aplite-hosted quartz UST layers in the Umnu Hutul W–Mo porphyry deposit (Fig. 1e) formed coevally with W mineralization (Table 2). At Oyu Tolgoi, Ridgeway, and

Hada Sumu, UST crystallization is co-genetic with abundant magnetite mineralization (Figs. 4c and 7b). In the case of Hada Sumu, even pure magnetite UST layers are developed (Kirwin 2005). The magnetite stage, however, predated the major Cu–Au mineralization at these localities.

Several authors agree that layered UST sequences, which commonly predate the major mineralizing events of depressurization-related quartz stockwork and breccia pipe formation, may act as chemical and physical barriers for circulating or passing mineralizing fluids (Lowenstern and Sinclair 1996; Kirwin 2005). Furthermore, UST occurrences on a district scale are direct field evidence for the presence of cupolas that are associated with over- pressured volatiles and fluids. Therefore, if USTs are observed, there is potential for the presence of a spectrum of intrusion-hosted and intrusion-related ore deposits. Based on our observations, depending on levels of uplift or erosion, breccia-hosted porphyry deposits might occur at topographically higher intervals, perhaps as much as 100 to 200 m above where the UST zone was exposed. Stockwork and disseminated mineralization, however, could be above, within, or below the UST horizon. In any case, the occurrence of USTs is considered to be a very favorable district-scale vector for intrusion-related mineral deposits.

Conclusions

The nine investigated localities of Asian and Australian porphyry and intrusion-related Au deposits and prospects revealed wide structural varieties of multiple-layered quartz UST sequences despite their overall similar structural appearance and spatial setting. In order to categorize the structural diversity, we suggest a classification and nomenclature for quartz UST sequences to provide a base for common terminology. We propose three structural groups: equigranular, heterogranular, and disturbed or disordered UST which are distinguished according to the UST layer shape or type of disorder:

1) Equigranular monomineralic quartz UST layers subdivided into straight, wavy, and contorted layer structure.
2) Heterogranular monomineralic quartz UST layers subdivided into straight, wavy, and contorted layer structure.
3) Disturbed or disordered USTs are equigranular or heterogranular USTs that are incompletely grown or ductile or brittle fragmented.

We suggest that the UST formation is the first stage of effective melt segregation from porphyry crystal mush and initiates the sequestering of metals from silica melts and their precipitation to form mineralized ore bodies in later stages. Based on our nine studied UST samples, most exhibit textural characteristics indicative of having crystallized initially from a silica melt. Three of them (Oyut Ulaan, Tampang, and Ridgeway) are interpreted to have formed coevally with fluid-vapor phase separation (open-system formation) and are co-genetic with chalcopyrite (Oyut Ulaan, and Tampang) and magnetite mineralization (Ridgeway). In the Tampang sample, "boiling" fluid inclusion assemblages were not observed but the simultaneous precipitation of UST quartz and chalcopyrite strongly suggests fluid-vapor phase separation during UST crystallization. Our data from the other localities are not conclusive, meaning that the UST sequence may have formed in an open-system environment or in a closed system. The closed-system model implies that UST layers crystallized either immediately below the upper contact to the wall rock due to undercooling or at a stock-internal contact of two porphyry phases in porphyry crustal mush. Based on such from our samples, we suggest that water and quartz-incompatible fluxes and phases that were released during the quartz crystallization accumulated in crystal mush interstices at the UST growth front and hindered the supply of silica for continuous quartz growth and crystal growth stopped. A new quartz nucleation interface formed at the water saturation front and the UST layer formation repeated. This process likely continued until either the system opened due to hydraulic collapse or the system ran out of volatiles. More than likely multiple explanations are possible.

Layered UST sequences are associated with over pressured volatiles and fluids, and their occurrence is considered to be a very favorable district-scale vector for intrusion-related mineral deposits where main mineralization might occur 100 to 200 m above the UST zone and minor mineralization is directly spatially associated with UST where UST acted as chemical and physical barriers for circulating and passing mineralizing fluids.

Acknowledgements We are very grateful to John Spratt from the Natural History Museum London who performed the quartz EPMA analyses. The authors acknowledge the constructive comments by Jacob B. Lowenstern and one anonymous reviewer who helped to clarify the presented data and resulting interpretations.

Funding Open access funding provided by University of Oslo (incl Oslo University Hospital) The study was financed by Ivanhoe Mines, Ltd. RS acknowledges funding under Natural Environment Research Council Grant NE/P017452/1: "From arc magmas to ores (FAMOS): A mineral systems approach."

Declarations

Conflict of interest The authors declare no competing interests.

Open Access This article is licensed under a Creative Commons Attribution 4.0 International License, which permits use, sharing, adaptation, distribution and reproduction in any medium or format, as long as you give appropriate credit to the original author(s) and the source, provide a link to the Creative Commons licence, and indicate if changes were made. The images or other third party material in this article are included in the article's Creative Commons licence, unless indicated otherwise in a credit line to the material. If material is not included in the article's Creative Commons licence and your intended use is not

permitted by statutory regulation or exceeds the permitted use, you will need to obtain permission directly from the copyright holder. To view a copy of this licence, visit http://creativecommons.org/licenses/by/4.0/.

References

Bain WM, Lecumberri-Sanchez P, Marsh EE, Steele-MacInnis M (2022) Fluids and melts at the magmatic-hydrothermal transition, recorded by unidirectional solidification textures at Saginaw Hill, Arizona, USA. Econ Geol 117:1543–1571. https://doi.org/10.5382/econgeo.4952

Baker EM, Andrew AS (1991) Geologic, fluid inclusion and stable isotope studies of the gold-bearing breccia pipe at Kidston, Queensland, Australia. Econ Geol 86:810–830

Bennett MM (2014) Cathodoluminescence and fluid inclusion characteristics of hydrothermal quartz from porphyry deposits. Dissertation, Colorado School of Mines

Blight JHS, Crowley QC, Petterson MG, Cunningham D (2010) Granites of the southern Mongolia Carboniferous arc: new geochronological and geochemical constraints. Lithos 116:35–52. https://doi.org/10.1016/j.lithos.2010.01.001

Bodnar RJ, Lecumberri-Sanchez P, Moncada D, Steele-MacInnis M (2014) Fluid inclusions in hydrothermal ore deposits. In: Holland HD, Turekian KK (eds) Treatise on Geochemistry, 2nd edn. Elsevier, Oxford, pp 119–142

Bodnar RJ, Vityk MO (1995) Interpretation of microthermometric data for H2O-NaCl fluid inclusions. In: De Vivo B, Frezzotti ML (eds) Fluid inclusions in minerals: methods and applications. Virginia Tech, Blacksburg, pp 117–130

Candela PA (1997) A review of shallow, ore-related granites: textures, volatiles, and ore metals. J Petrol 38:1619–1633

Candela PA, Blevin PL (1995) Do some miarolitic granites preserve evidence of magmatic volatile phase permeability? Econ Geol 90:2310–2316

Carter LC, Williamson BJ (2022) Textural indicators of mineralisation potential in porphyry magmatic systems – a framework from the archetypal Yerington district, Nevada. Ore Geol Rev 143:104783

Cernuschi F, Dilles JH, Grocke SB, Valley JW, Kitajima K, Tepley FJ (2018) Rapid formation of porphyry copper deposits evidenced by diffusion of oxygen and titanium in quartz. Geology 46:611–614

Crane D, Kavalieris I (2012) Geologic overview of the Oyu Tolgoi porphyry Cu-Au-Mo deposits, Mongolia. In: Hedenquist JW, Harris M, Camus F (eds) Geology and Genesis of Major Copper Deposits and Districts of the World - A tribute to Richard H Sillitoe, SEG Spec Publ 16, pp 187–213

Dingwell DB (1988) The structures and properties of fluorine-rich magmas: a review of experimental studies. In: Taylor RP, Strong DF (eds) Recent Advances in the Geology of Granite-related Mineral Deposits. CIM SPEC vol 31, pp 1–12

Erdenebayar J, Ogata T, Imai A, Sereenen J (2014) Textural and chemical evolution of unidirectional solidification textures in highly differentiated granitic rocks at Kharaatyagaan, Central Mongolia. Resour Geol 64:283–300. https://doi.org/10.1111/rge.12050

Fenn PM (1986) On the origin of graphic granite. Amer Mineral 71:325–330

Forbes CN, License P, Panther CA (2003) Initial follow-up sampling program, Hada Sumu gold-copper prospect, Saihan Ta La region, Inner Mongolia, China. Technical Report Ivanhoe Mines Ltd., Adelaide

Goldstein RH (2003) Petrographic analysis of fluid inclusions. In: Samson I, Anderson A, Marshall D (eds) Fluid inclusions: Analysis and interpretation. Miner Ass Canada, Short Course Series Vol 32, pp 9–53

Gustafson LB, Hunt JP (1975) The porphyry copper deposit at El Salvador, Chile. Econ Geol 70:857–912

Halls C (1994) Energy and mechanism in the magmato-hydrothermal evolution of the Cornubian Batholith: a review. In: Möller P, Kämpf H (eds) Seltmann R. Metallogeny of collisional orogens, Czech Geol Surv Prague, pp 275–294

Hayden LA, Watson EB (2007) Rutile saturation in hydrous siliceous melts and its bearing on Ti-thermometry of quartz and zircon. EPSL 258:561–568

Hedenquist JW, Arribas A, Reynolds TJ (1998) Evolution of an intrusion-centered hydrothermal system; Far Southeast-Lepanto porphyry and epithermal Cu-Au deposits, Philippines. Econ Geol 93:373–404

Heinrich CA, Günther D, Audétat A, Ulrich T, Frischknecht R (1999) Metal fractionation between magmatic brine and vapor, determined by microanalysis of fluid inclusions. Geology 27:755–758

Holliday JR, Wilson AJ, Blevin PL, Tedder IJ, Dunham PD, Pfitzner M (2002) Porphyry gold-copper mineralization in the Cadia district, eastern Lachlan fold felt, New South Wales, and its relationship to shoshonitic magmatism. MineralDeposita 37:100–116. https://doi.org/10.1007/s00126-001-0233-8

Huang R, Audétat A (2012) The titanium-in-quartz (TitaniQ) thermobarometer: a critical examination and re-calibration. Geochim Cosmochim Acta 84:75–89

Huang K, Zhu M, Zhang L, Bai Y, Cai Y (2020) Geological and mineralogical constraints on the genesis of the Bilihe gold deposit in Inner Mongolia, China. Ore Geol Rev 124:103607

Khashgerel B-E, Rye RO, Kavelieris I, Hayashi K (2009) The sericitic to advanced argillic transition: stable isotope and mineralogical characteristics from the Hugo Dummett porphyry Cu-Au deposit, Oyu Tolgoi district, Mongolia. Econ Geol 104:1087–1110. https://doi.org/10.2113/gsecongeo.104.8.1087

Kirkham RV, Sinclair WD (1988) Comb quartz layers in felsic intrusions and their relationship to the origin of porphyry deposits. In: Taylor RP, Strong DF (eds) Recent Advances in the Geology of Granite-related Mineral Deposits, Canadian Inst Mining Metallurgy, Special Vol 39:50–71

Kirwin DJ (2001) Report on an inspection of Bongkud porphyry copper gold project, Ranau district, Sabah, East Malaysia. Technical Report Ivanhoe Mines Ltd., Adelaide

Kirwin DJ (2005) Unidirectional solidification textures associated with intrusion-related Mongolian mineral deposits. In: Seltmann R, Gerel O, Kirwin DJ (eds) eodynamics and Metallogeny of Mongolia with a Special Emphasis on Copper and Gold Deposits. Centre for Russian and Central Eurasian Mineral Studies, IAGOD Guidebook Series 11, London, pp 63–84

Kirwin DJ (2006) Unidirectional solidification textures, miarolitic cavities and orbicles: field evidence for the magmatic to hydrothermal transition in intrusion-related mineral deposits. Presentation at SEEGF conference October 2006. http://www.cmi-capital.com/Doc_Server/SEEGF_Docs/Kirwin/2-UST-Europe-10%20Sep%202006.pdf. Accessed Jan 21 2021

Kirwin DJ, Seltmann R (eds) (2002). Extended Abstracts, 11th Quadrennial IAGOD Symposium and Geocongress, Geol Surv Namibia, Windhoek, pp 22–26

Kirwin DJ, Foster CN, Kavalieris I, Grane D, Orssich C, Panther C, Gramajav D, Munkhbat TO, Niiselekhuu G (2005) The Oyu Tolgoi copper-gold porphyry deposits, south Gobi, Mongolia. In: Seltmann R, Gerel O, Kirwin D (eds) Geodynamics and Metallogeny of Mongolia with a Special Emphasis on Copper and Gold Deposits, Centre for Russian and Central Eurasian Mineral Studies, IAGOD Guidebook Series 11, London, pp 155–168

Knipping JL, Bilenker LD, Simon AC, Reich M, Barra F, Deditius AP, Lundstrom C, Bindeman I, Munizaga R (2015) Giant Kiruna-type deposits form by efficient flotation of magmatic magnetite suspensions. Geology 43:591–594

Koděra P, Kozák J, Brčeková J, Chovan M, Lexa J, Jánošík M, Biroň A, Uhlík P, Bakos F (2018) Distribution and composition of gold in porphyry gold systems: example from the Biely Vrch deposit, Slovakia. Miner Deposita 53:1193–1212

Koval PV, Ariunbileg S, Libatorov YuI, Maksimyuk UE (1988) The Bayan-Uul porphyry copper-molybdenum occurrence and relation to magmatism, central Mongolia. Geol Ore Deposits 3:24–35

Lamb MA, Cox D (1998) New $^{40}Ar/^{39}Ar$ age data and implications for porphyry copper deposits of Mongolia. Econ Geol 93:524–529. https://doi.org/10.2113/gsecongeo.93.4.524

Landtwing MR, Pettke T (2005) Relationships between SEM-cathodoluminescence response and trace-element composition of hydrothermal vein quartz. Amer Mineral 90:122–131

London D (1992) The application of experimental petrology to the genesis and crystallisation of granitic pegmatites. Can Miner 30:499–540

London D (2009) The origin of primary textures in granitic pegmatites. Can Miner 47:697–724. https://doi.org/10.3749/canmin.47.4.697

London D (2014) A petrologic assessment of internal zonation in granitic pegmatites. Lithos 184–187:74–104

Lowenstern JB, Sinclair WD (1996) Exsolved magmatic fluid and its role in the formation of comb-layered quartz at the Cretaceous Logtung W-Mo deposit, Yukon Territory, Canada. Trans Royal Soc Edinburgh 87:291–303

Malekzadeh Shafaroudi A, Karimpour MH, Stern CR (2015) The Khopik porphyry copper prospect, Lut Block, Eastern Iran: Geology, alteration and mineralization, fluid inclusion, and oxygen isotope studies. Ore Geol Rev 65:522–544. https://doi.org/10.1016/j.oregeorev.2014.04.015

Mao W, Rusk B, Yang F, Zhang M (2017) Physical and chemical evolution of the Dabaoshan porphyry Mo deposit, south China: insights from fluid inclusions, cathodoluminescence, and trace elements in quartz. Econ Geol 112:889–918

Maydagán L, Franchini M, Rusk B, Lentz DR, McFarlane C, Impiccini A, Rios FJ, Rey R (2015) Porphyry to epithermal transition in the Altar Cu-(Au-Mo) deposit, Argentina, studied by cathodoluminescence, LA-ICP-MS, and fluid inclusion analysis. Econ Geol 110:889–923

Mernagh TP, Mavrogenes J (2019) Significance of high temperature fluids and melts in the Grasberg porphyry copper-gold deposit. Chem Geol 508:210–224

Müller A, Herrington R, Armstrong R, Seltmann R, Kirwin DJ, Stenina NG, Kronz A (2010) Trace elements and cathodoluminescence of quartz in stockwork veins of Mongolian porphyry-style deposits. Mineral Deposita 45:707–727. https://doi.org/10.1007/s00126-010-0302-y

Murgulov V, Griffin WL, O'Reilly SY (2009) Temporal and genetic relationships between the Kidston gold-bearing Breccia Pipe and the Lochaber Ring Dyke Complex, North Queensland, Australia: insights from in situ U-Pb and Hf-isotope analysis of zircon. Mineral Petrol 95:17–45. https://doi.org/10.1007/s00710-008-0020-7

Mustard R (2001) Granite-hosted gold mineralization at Timbarra, northern New South Wales, Australia. Mineral Deposita 36:542–562. https://doi.org/10.1007/s001260100188

Perelló J, Cox D, Garamjav D, Sanjdorj S, Diakov S, Schissel D, Munkhbat T-O, Oyun G (2001) Oyu Tolgoi, Mongolia - Silurian-Devonian porphyry Cu-Au-(Mo) and high-sulfidation Cu mineralization with a Cretaceous chalcocite blanket. Econ Geol 96:1407–1428. https://doi.org/10.2113/gsecongeo.96.6.1407

Porter TM (2016) The geology, structure and mineralisation of the Oyu Tolgoi porphyry copper-gold-molybdenum deposits, Mongolia: a review. Geosci Front 7:375–407

Richards JP (2005) Cumulative factors in the generation of giant calc-alkaline porphyry Cu deposits. In: Porter TM (ed) Super porphyry copper and gold deposits: A global perspective, vol 1. PGC Publishing, Adelaide, pp 7–25

Roedder (1984) Fluid inclusions. Miner Soc Am Rev Miner 12:644

Rottier B (2016) Magmatic and hydrothermal fluid processes at the origin of the giant porphyry-related epithermal polymetallic deposit of Cerro de Pasco (central Peru). Dissertation, University of Geneva

Rottier B, Casanova V (2021) Trace element composition of quartz from porphyry systems: a tracer of the mineralizing fluid evolution. Mineral Deposita 56:843–862

Rottier B, Kouzmanov K, Casanova C, Bouvier A-S, Baumgartner L, Wälle M, Fontboté L (2018) Hydrothermal evolution of a hidden porphyry-type mineralization related to the large epithermal polymetallic deposit of Cerro de Pasco district (Peru). Mineral Deposita 53:919–946

Rusk B (2012) Cathodoluminescent textures and trace elements in hydrothermal quartz. In: Götze J, Möckel R (eds) Quartz: Deposits. Mineralogy and Analytics, Springer, Heidelberg, New York, pp 307–329

Rusk BG, Lowers HA, Reed MH (2008) Trace elements in hydrothermal quartz: relationships to cathodoluminescence textures and insights into vein formation. Geology 36:547–550

Seedorff E, Dilles JH, Proffett JM Jr, Einaudi MT, Zurcher L, Stavast WJA, Johnson DA, Barton MD (2005) Porphyry deposits: characteristics and origin of hypogene features. In: Hedenquist JW, Thompson JFH, Goldfarb RJ, Richards JP (eds) Economic Geology 100th Anniversary volume. Society of Economic Geologists, Littleton, pp 251–298

Seo JHu, Kim Y, Lee T, Guillong M (2021) Periodically released magmatic fluids create a texture of unidirectional solidification (UST) in ore-forming granite: a fluid and melt inclusion study of W-Mo forming Sannae-Eonyang Granite, Korea. Minerals 11:888. https://doi.org/10.3390/min11080888

Shannon JR, Walker BM, CartenRB GEP (1982) Unidirectional solidification textures and their significance in determining relative ages of intrusions at the Henderson Mine, Colorado. Geology 10:293–297

Sillitoe RH (2010) Porphyry copper systems. Econ Geol 105:3–41

Sinclair WD (2007) Porphyry deposits. In: Goodfellow WD (ed) Mineral Deposits of Canada: A Synthesis of Major Deposit-Types, District Metallogeny, the Evolution of Geological Provinces, and Exploration Methods, Geological Association of Canada, Mineral Deposits Division, Special Publ No. 5, pp 223–243

Tanner D, Henley RW, Mavrogenes JA, Holden P (2013) Combining in situ isotopic, trace element and textural analyses of quartz from four magmatic-hydrothermal ore deposits. Contrib Mineral Petrol 166:1119–1142

Tsuruoka S (2017) he evolution of hydrothermal fluids from the deep porphyry environment to the shallow epithermal environment. Dissertation, Colorado School of Mines

Wilkinson JJ (2013) Triggers for the formation of porphyry deposits in magmatic arcs. Nat Geosci 6:917–925

Wilson AJ, Cooke DR, Harper BL (2003) The Ridgeway gold-copper deposit: a high-grade alkalic porphyry deposit in the Lachlan fold belt, New South Wales, Australia. Econ Geol 98:1637–1666. https://doi.org/10.2113/gsecongeo.98.8.1637

Wilson AJ, Cooke DR, Stein HJ, Fanning MC, Holliday JR, Tedder IJ (2007) U-Pb and Re-Os geochronologic evidence for two alkalic porphyry ore-forming events in the Cadia district, New South Wales, Australia. Econ Geol 102:3–26. https://doi.org/10.2113/gsecongeo.102.1.3

Yang K, Bodnar RJ (1994) Magmatic-hydrothermal evolution in the "bottoms" of porphyry copper systems: evidence from silicate melt and aqueous fluid inclusions in granitoid intrusions in the Gyeongsang Basin, South Korea. Inter Geol Rev 36:608–628

Zhang L, Xiao W, Qin K, Zhang Q (2006) The adakite connection of the Tuwu-Yandong copper porphyry belt, eastern Tianshan, NW China -trace element and Sr-Nd-Pb isotope geochemistry. Mineral Deposita 41:188–200. https://doi.org/10.1007/s00126-006-0058-6

Publisher's note Springer Nature remains neutral with regard to jurisdictional claims in published maps and institutional affiliations.